Summer 2016

Microbubble Generation By Piezoelectric Transducers For Biomedical Studies

Mohammed Alkhazal
Old Dominion University

MICROBUBBLE GENERATION BY PIEZOELECTRIC TRANSDUCERS FOR BIOMEDICAL STUDIES

by

Mohammed Alkhazal
B.S. December 2014, Old Dominion University

A Thesis Submitted to the Faculty of
Old Dominion University in Partial Fulfillment of the
Requirements for the Degree of

MASTER OF SCIENCE

ELECTRICAL AND COMPUTER ENGINEERING

OLD DOMINION UNIVERSITY
August 2016

Approved by:

Shu Xiao (Director)

Gon Namkoong (Member)

Chunqi Jiang (Member)

ABSTRACT

MICROBUBBLE GENERATION BY PIEZOELECTRIC TRANSDUCERS FOR BIOMEDICAL STUDIES

Mohammed Alkhazal
Old Dominion University, 2016
Director: Shu Xiao

Bubbles induced by blast waves or shocks are speculated as the major cause of damage in biological cells in mild traumatic brain injuries (TBI). Microbubble collapse was found to induce noticeable cell detachment from the cell substrate, changes in focal adhesion, and biomechanics. To better understand the bubble mechanism, a system needs to be constructed which allows clear differentiation on the impact of bubbles from that of shocks. Such a generator needs to be low profile in order to place under a microscope. A piezoelectric transducer system was designed to meet the need. The system uses either a flat or a spherical focusing piezoelectric transducer to produce microbubbles in a cuvette loaded with cell-culture medium. Several transducer configurations were designed and tested. The first design has a transducer that faces upward in a water chamber, so that the pressure waves can reach a coverslip placed above the transducer. To allow for the light passage, the transducer was drilled at the center and a hole was created. This configuration was found not easy to use as it created water jets at the water surface when water level was shallow. A second configuration where the transducer was placed on the side of the cuvette with its axis lining horizontally was then designed. A cover slip was placed on the top of the cuvette. The impact of the waves to the cells was minimized as the cover slip was parallel to the direction of the wave. Only bubbles from the medium could reach the cover slip and interact with cells. The effect of bubbles, therefore, can be separated that of pressure waves. The bubbles collected on a cover slip range in size from 10 μm to 100 μm in radius, but the dominant size is 10-30 μm.

This thesis is dedicated to my daughter, wife, and family.

ACKNOWLEDGMENTS

During my time as a graduate student at Old Dominion University, my advisor Dr. Shu Xiao has been a tremendous influence. His research captured my interest and I will be always honored to be one of his students. He always offered his support, knowledge, and experience and I'm forever in debt for his patience and help, my sincere gratitude goes to him. He also introduced me to Dr. Wei-Dong Zhu who has helped me with this project with his ideas and experiences.

I also thank my family for providing me with endless support toward achieving my life goals and pursuing my interests.

This work was supported by a grant (N00014-13-1-0404) from the Office of Naval Research.

TABLE OF CONTENTS

Page

LIST OF TABLES viii

LIST OF FIGURES ix

Chapter

1. INTRODUCTION 1
2. OVERVIEW OF SHOCK WAVE GENERATORS 4
   - 2.1 Laser Induced Shock Waves 4
   - 2.2 Shock-Tubes 5
   - 2.3 Spark Gap Discharges 7
3. PIEZOELECTRICITY 11
   - 3.1 Piezoelectricity Theory 11
   - 3.2 Equivalent Circuit Models 15
4. MEASUREMENT OF PRESSURE 17
   - 4.1 Piezoelectric Pressure Sensor 17
   - 4.2 Fiber Optic Hydrophone 19
   - 4.3 Preparation and Calibration 20
5. PIEZOELECTRIC TRANSDUCER DEVICES 23
   - 5.1 Power Amplifier 23
   - 5.2 Push-Pull Circuit 24
   - 5.3 Self-Resonance Circuit 26
6. PIEZOELECTRIC MICROBUBBLE GENERATOR 29
   - 6.1 Transducers 29
   - 6.2 Chamber Design 32
     - 6.2.1 Transducer with Aperture 32
     - 6.2.2 Two Transducers at an Angle 33
     - 6.2.3 Transducer Mounted on the Side 34
   - 6.3 Final Package 36
7. EXPERIMENTAL RESULTS 38
   - 7.1 Pressure Analysis 38
     - 7.1.1. Push-Pull Driven Transducers 39
     - 7.1.2 Transducers Driven by Self-Resonance Driver 45

7.1.3 Bubble Generation 47
7.1.4 Bubbles on the Cover Slip 49
8. DISCUSSION 58
8.1 The Negative Impact of Increasing Driver Voltage 58
8.2 The Choice of Driver's Frequency 59
8.3 Bubble Growth 59
9. SUMMARY AND CONCLUSIONS 63
REFERENCES 64
APPENDIX A 70
VITA 78

LIST OF TABLES

Table page

Physical meaning of the partial derivatives of the internal energy 72
Piezoceramic discs characterizing coefficients (Thickness vibration mode) 76

LIST OF FIGURES

Figure page

1. Cavitation bubble collapse forming a microjet. 2
2. Shock wave and bubble generation after a 35 femtoseconds, 2 mJ pulsed laser incident on air-water interface. The scale bar in the low right corners are 200 μm. (a) Ionization at and beneath the surface. (b) Plasma expansion from the surface. (c) Generation of shockwaves both above and below the surface. (d) Cavity formation at the surface. (e) Cavity closure and bubble formation [14]. 5
3. Shock waves generated inside a shock tube [16]. 6
4. Electric pulse compression: (a) input pulse and (b) output pulse [17] © 2000 IEEE. 7
5. A Marx generator circuit diagram [17] © 2000 IEEE. 8
6. A pulse forming line circuit diagram [17] © 2000 IEEE. 9
7. A solid state high voltage generator [11] © 2014 IEEE. 10
8. Laser shadow graphs of a 4 kV water discharge creating a shock wave and cavitation bubbles [11] © 2014 IEEE. 10
9. Vibration modes of ceramics. 12
10. PZT under external polarizing electric field [22]. 14
11. Van Dyke model [24] © 2008 IEEE. 15
12. Extended Dyke model [24] © 2008 IEEE. 16
13. Photo of (a) a signal conditioner and (b) a piezoelectric pressure sensor. 18
14. The internal components of PCB 113B24. 18
15. ONDA HFO-690 fiber optic hydrophone (pressure sensor). 19
16. Pressure measurement using fiber optic hydrophone. 20
17. The preparation of using fiber optic hydrophone. 21
18. A simple testing setup that has an off-the-shelf broadband amplifier. 23
19. The Push-Pull circuit. 24
20. The voltage that delivers to the load. 25
21. The voltage and current have a period of 2.1 MHz. 25
22. A self-resonance circuit used in an atomizer [30]. 27
23. The voltage in the self-resonance circuit. 28
24. The voltage and current in the self-resonance circuit. 28
25. Piezoelectric transducers, spherical disc (right) and flat disc (left). 30
26. The experimental setup used for capturing bubbles. 30
27. Bubble production in a 1.6 s span. 31
28. Stacking transducers. 32
29. Transducer with an aperture 33
30. Two transducers combine the pressure at the sample location. 34
31. A bubble chamber that has a piezoelectric transducer placed sideway. 35
32. Final chamber fabricated with 1 mm thick glass sheets was placed under a 40X objective lens. 36
33. The whole setup of the bubble generator, which includes the driver, the chamber, and the microscope. 37
34. The setup for measuring pressure. Left: the controller for the hydrophone and the oscilloscope. Right: a water tank and a 3 axis maneuver stage that holds the fiber. 38

35. Pressure waves generated by the spherical transducer at its focal point. 40
36. Pressure waves can be plotted in a synchronous way that shows fairly consistent peaks for a spherical transducer. The onsets of the pressure waves are not shown. 41
37. The probability of positive onset versus pulse width. 41
38. Vertical pressure distribution – flat transducer. 42
39. Vertical pressure distribution – spherical transducer. 43
40. Lateral pressure distribution – spherical transducer. 43
41. Vertical pressure distribution – spherical transducer with an aperture. 44
42. Lateral pressure distribution – spherical transducer with an aperture. 44
43. The pressure at the focal distance of 30 mm produced by the spherical transducer driven by the self-resonance circuit. 46
44. Pressure distribution for spherical and flat transducers. 46
45. Snapshots of the chamber (a) before and (b) after bubble generation 48
46. A still image of the microbubbles generated in tap water. A needle with a diameter of 190 µm was placed as a scale [30]. 49
47. Two images captured within a second showing that bubbles cluster after reaching the cover slip. 50
48. Summation of 17 images showing different bubble sizes. 51
49. Histogram of the bubble radii of the superimposed image in figure 35. 51
50. Histogram graphs for (a) 5 seconds shot, (b) 10 seconds shot, (c) 15 seconds shot, and (d) 20 seconds shot. 52
51. Photo montage of two bubbles collapsing at the surface of the chamber [30]. 53
52. Time dependence of the radius of the cross-sectional circle [30]. 54
53. Time dependence of the evaluated bubbles' volumes [30]. 55
54. Radial collapsing speed versus the radius of the cross-sectional circle. As the bubble becomes smaller, the faster it collapses [30]. 55
55. Condencation inside a bubble. 56
56. Smaller bubbles embedded in the walls of bigger bubbles. 57
57. Electrolysis bubbles coming from a transducer after a 100 ms pulse. 58
58. Nodes and antinodes of a sinusoidal standing wave [35]. 61
59. The effect of poling on polarization domains. (a) Unpoled (b) Poled. 75
60. One-dimensional model of a thickness vibration mode piezoceramic. 75

CHAPTER 1

INTRODUCTION

Shock wave generators are useful for medical treatments and research such as kidney stone treatment (lithotripsy) [1], tumor destruction [2], drug delivery [3], or other biomedical applications. A shock wave is a high gradient pressure wave that contains a compressive phase (positive pressure) and a tensile phase (negative pressure) [4]. Such an abrupt transition in pressure in a liquid medium could induce microbubbles or cavitation bubbles. They are defined as the creation of vapor cavities within a liquid medium under low pressure. Small air pockets usually exist in the liquid. The compression and subsequent expansion of the air pockets cause the formation of cavitation bubbles. When these cavitation bubbles collapse, microjets can form as the liquid rushes into the cavity (Figure 1) [5]. The cavitation bubbles have been reported throughout history as a major culprit in posing harms to propellers, pumps, and hydro turbines [6].

Shock waves and cavitation bubbles are also linked to the blast-traumatic brain injury (bTBI) [7], which is mainly caused by sudden impact of blast waves on the brain due to explosions such as improvised explosive devices (IEDs) [8]. In the human's head there are several tissue types and each has its own acoustic impedance. When a shock wave travels through different tissues, fragmentation (spallation) of tissue occurs as a result of the mismatch of acoustic impedances. The blast wave causes abrupt change in the intracranial pressure which induces bubbles at the interface between the cerebrospinal fluid (CSF) and the brain. Moreover, simulations suggest that skull deformation with elastic rebound is one of the factors that cause cavitation bubbles [9].

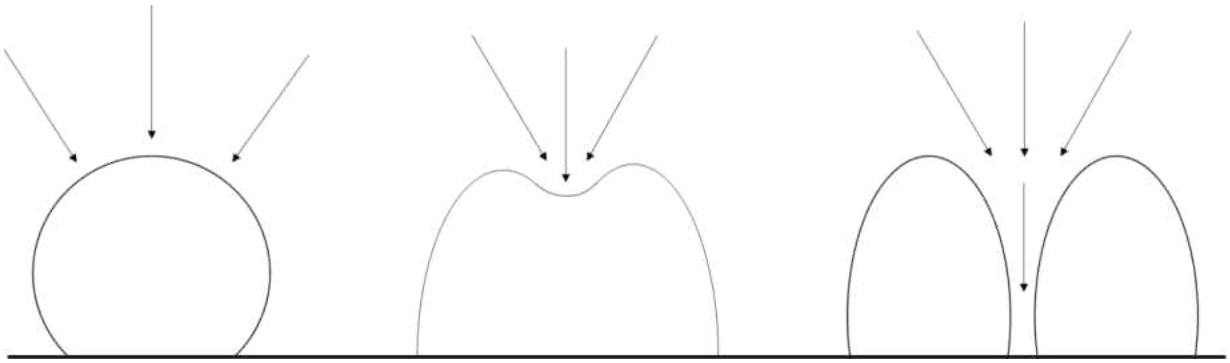

Figure 1. Cavitation bubble collapse forming a microjet.

Despite the popular view of the role of cavitation bubbles in the deleterious effects associated with shock waves, there hasn't been any concrete evidence that shows a clear presence of cavitation in human or animal heads subjected to shock impact. Therefore, the research of interaction of shock wave and biological matter has been ongoing. Experimental shock and blast systems that can be repeatedly applied repeatedly are needed to conduct the research. It will be more beneficial if such a system can be operated on a microscope.

Shock waves can be generated by high energy laser short pulses, shock tubes, high voltage spark gap discharges, and piezoelectric transducers. Each method has its own characteristics. For instance, laser induced shock wave produce a single shock inducing a single bubble. To produce multiple bubbles, multiple lasers have to be used [10], and it is not so efficient as it will add more complexity. Shock tubes are very good at mimicking an actual explosion, but they are far too large to be used under microscopes. High voltage spark gap discharge systems are easy to build and can be done with a great deal of control, but they generate a high electric field just before breakdown which might be a source of artifact. Although there is no evidence of such artifact reported ([7] and [11]), it is still desired to reduce the electric field. Furthermore, it is not clear whether shock

waves are always coupled with cavitation bubbles. Previously, it was also reported that high voltage spark gap discharges are quite effective in generating microbubbles for biological studies under a microscope. Shock waves alone were not effective at inducing damage to the cells and it was the bubbles that caused the damage [7]. But it is still not clear that cavitation alone would undertake the role. As shock wave generators produce spherical shocks that always reach the biological sample of interest, it is difficult to separate the shock wave from the cavitation bubbles in time.

As a result, low voltage piezoelectric transducers become the top candidate to experiment in that 1) they operate at much lower electric fields in comparison with spark gap systems and they are proven to produce cavitation bubbles in applications such as ultrasonic baths and vaporizers (atomizers); and 2) the bubbles can be produced by oscillation waves that have a much lower intensity. It becomes possible to separate pressure waves from bubbles.

On these bases, this thesis is focused on creating a cavitation generator that is driven by piezoelectric transducers, allowing biologists to study the effects of microbubbles of biological specimen at the cellular level on a microscope.

CHAPTER 2

OVERVIEW OF SHOCK WAVE GENERATORS

In this chapter, an overview of the shock wave generators used in the biomedical field is given. Used in studying the effects of shocks and cavitation bubbles on the microscopic level, they assist biologists in understanding the comprehensive impact of bTBI human cells and tissue. Laser induced shock waves, shock tubes, and spark gap shock wave generators are overviewed. Later in Chapter 3, piezoelectric transducers will be discussed.

2.1 Laser Induced Shock Waves

Laser systems can be used to generate shock waves in a liquid medium. Short and powerful pulses that are typically few nanoseconds down to femtoseconds are focused in the liquid, leading to optical breakdown and consequently generating a shock wave that propagate through the liquid. Immediately after, a cavitation bubble is generated (Figure 2).

Similar to the laser ablation process, focused laser pulses deposit large energy in the liquid during a short time interval. The required power intensity for such laser beam has to be 10^8 W/cm^2 or higher in order to generate optical breakdown, shock wave and cavitation bubble [12]. A laser-induced breakdown in the liquid media is the result of electron cascade ionization or direct ionization (multiphoton ionization). For electron cascade ionization to occur, free electrons have to be present. They absorb laser photons during collisions with heavy particles (inverse Bremsstrahlung absorption). When a free electron gains enough energy to ionize bound electrons, it collides with a water molecule which results in two free electrons of lower energies. The repetition of this process creates enough free electrons leading to breakdown and plasma

formation. The generated plasma expands at the supersonic velocity compressing the surrounding liquid and thus creates a shock wave [13].

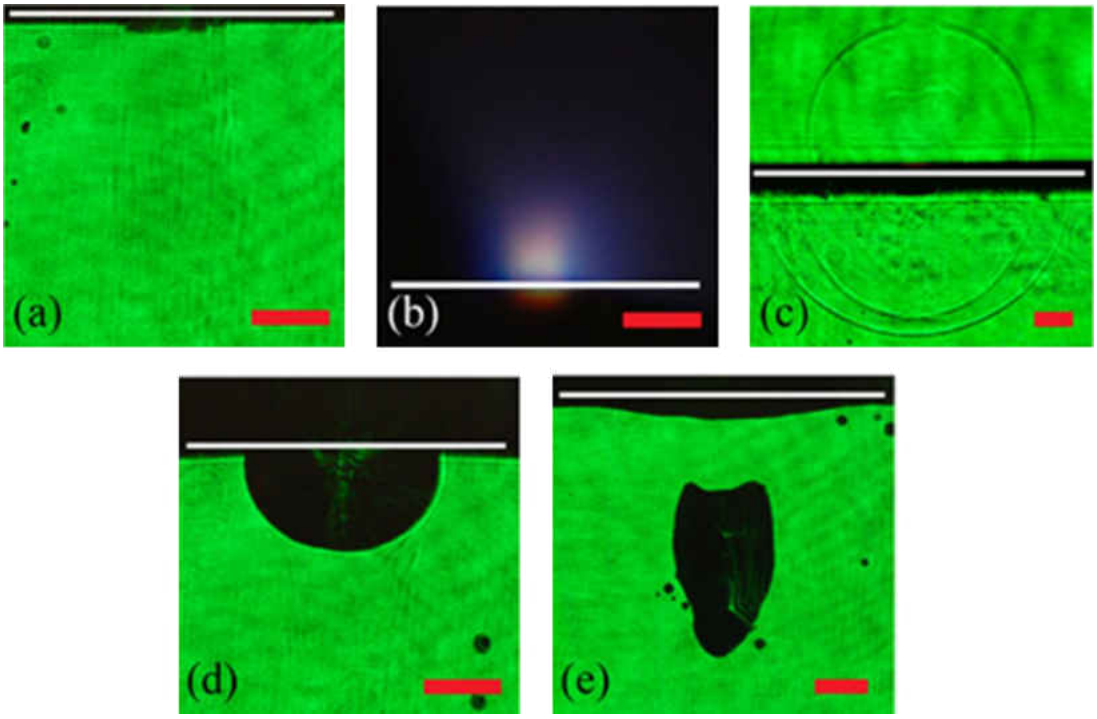

Figure 2. Shock wave and bubble generation after a 35 femtoseconds, 2 mJ pulsed laser incident on air-water interface. The scale bar in the low right corners are 200 µm. (a) Ionization at and beneath the surface. (b) Plasma expansion from the surface. (c) Generation of shockwaves both above and below the surface. (d) Cavity formation at the surface. (e) Cavity closure and bubble formation [14].

2.2 Shock-Tubes

Shock tubes can be driven either by high pressure compression or explosion. Compression shock tubes consist of two sections of different pressures (high and low) that are separated by a

diaphragm. When the pressure inside the highly pressurized section reaches a certain threshold, the diaphragm ruptures or alternatively, the diaphragm could be ruptured by a mechanical device, and the compressed air rushes down to the low pressure section creating a shock wave [15]. Explosion-based shock tubes can be driven by a variety of explosive materials. These shock tubes are fairly easy to build, but their large scale presents challenges for adapting them to the microscope. Moreover, compared to spark gap generators and piezoelectric transducers, they need frequent maintenance as the diaphragm has to be replaced from shot to shot.

A shock tube produces complex shock waves other than the leading shock wave that mimics the shock wave of a typical blast in the free space (Figure 3). These complex shock waves include reflected shock waves in the tube wall, a turbulent jet, Mach stem (shock wave formed from shock reflections), and rarefaction waves. The problem in having these byproducts is that they will cause more damage than what is typical for primary bTBI, which may lead the studies into false-positive results that would rarely happen in actual bTBI injuries [16].

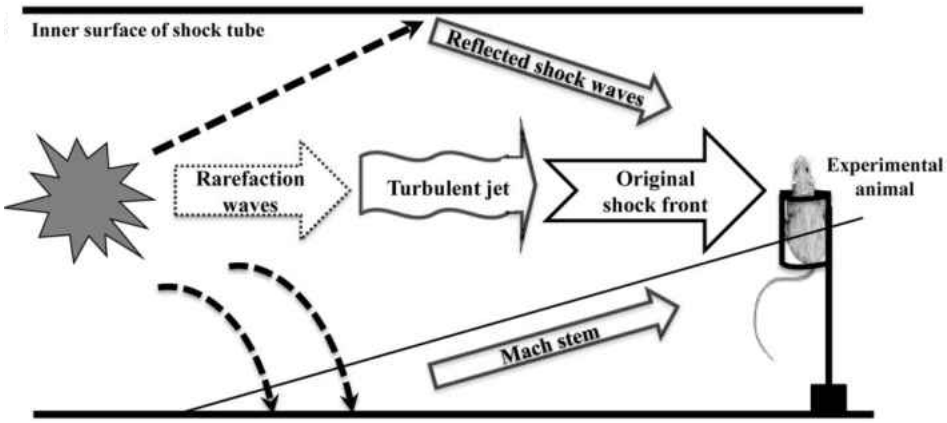

Figure 3. Shock waves generated inside a shock tube [16].

2.3 Spark Gap Discharges

Spark gap shock wave generators are convenient for microscope studies because the discharging electrodes can be made small. Electrodes are driven by high voltage electric pulses and create breakdowns, which subsequently generate a shock wave and microbubbles (Figure 8). Such a system can be made in a variety of configurations for different output powers and compactness. The most frequently-used high voltage pulse generator is a capacitive discharge system, where a capacitor delivers the current to the load after a switch being turned on. The capacitive discharge system can be a Marx generator, a pulse forming line, or a solid state generator. The general idea is to convert low power charging to high power discharging. For example, a total power of 1 kW charged to a capacitor over 1 s can be turned to 1 GW output over 1 μs if there is no loss (Figure 4).

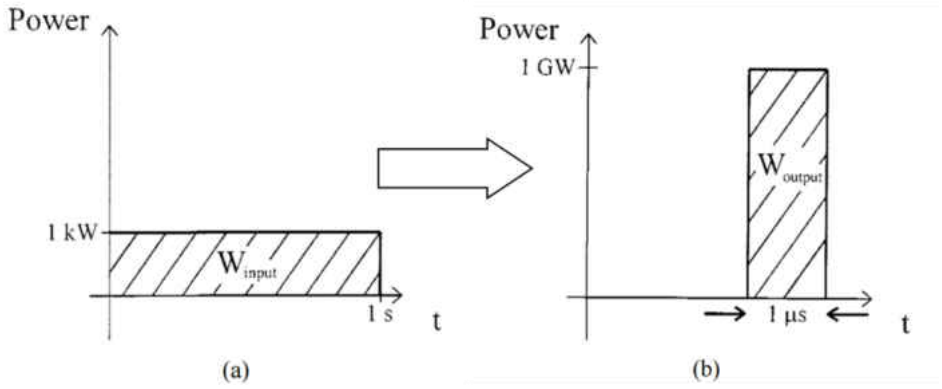

Figure 4. Electric pulse compression: (a) input pulse and (b) output pulse [17] © 2000 IEEE.

Marx generators are quite popular for generating high voltages for a variety of purposes such as lightning strike testing and biomedical applications. Parallel capacitors are charged by a DC high voltage source and discharged through a series of switches and so the output voltage is multiplied by the number of stages after all switches close (Figure 5).

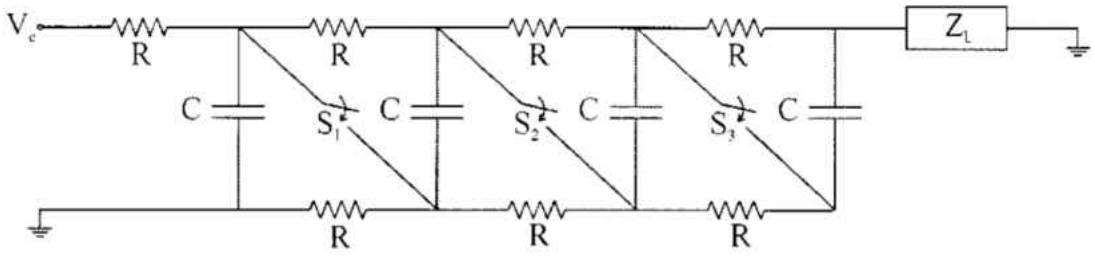

Figure 5. A Marx generator circuit diagram [17] © 2000 IEEE.

Transmission line or pulse forming line generators are very commonly used in laboratories due to the ease of construction and effectiveness in generating short pulses. Its basic circuit is shown in Figure 6. A high voltage charging source with a voltage V_0 is connected to a transmission line of length d. When the line is charged and the switch closes at t_0, the line discharges into the load resistance that is matched to the impedance of the line. Taking into account the waves that propagate in two directions and each having a voltage of $V_0/2$, a step voltage of $V_0/2$ will be launched towards the load. The total pulse duration is:

$$t = \frac{2d\sqrt{\epsilon_r}}{c} \tag{1}$$

where ϵ_r is the relative permittivity of the insulator of the line and c is the speed of light.

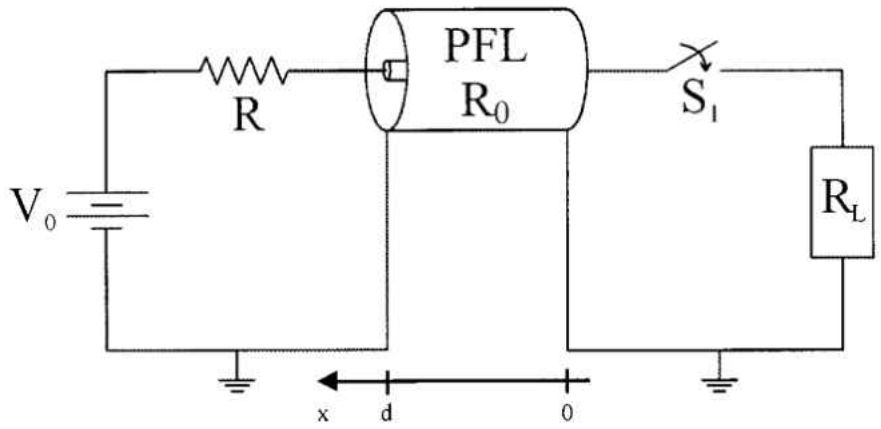

Figure 6. A pulse forming line circuit diagram [17] © 2000 IEEE.

Solid state high voltage pulse generators are based on the same concept of Marx generators. Using controllable switches such as MOSFETs or BJTs, the Marx can generate pulses with varying pulse duration. As each switch is only capable of handling approximately 1 kV, the Marx configuration allows for a voltage boost. Another configuration to increase the voltage is to directly stack the switches in series. Each switch is connected a pre-charged capacitor, which will discharge to the gate of the switch sequentially starting from the bottommost switch. One of the examples is shown in Figure 7 [11]. Power MOSFETs were used. The circuit uses a gate driver for the bottom MOSFET. When a driving pulse is sent to the gate of the MOSFET, the MOSFET is turned on and opens a current path for the capacitor connected to the above MOSFET. The capacitor charges the gate. But the gate-source voltages clamped via a Zener diode. This action keeps going until all the MOSFETs are turned on. As a result, a 4 kV pulse is formed to deliver to the spark gap electrodes, creating a breakdown in water. Shock waves and bubbles are observed following the breakdown (Figure 8).

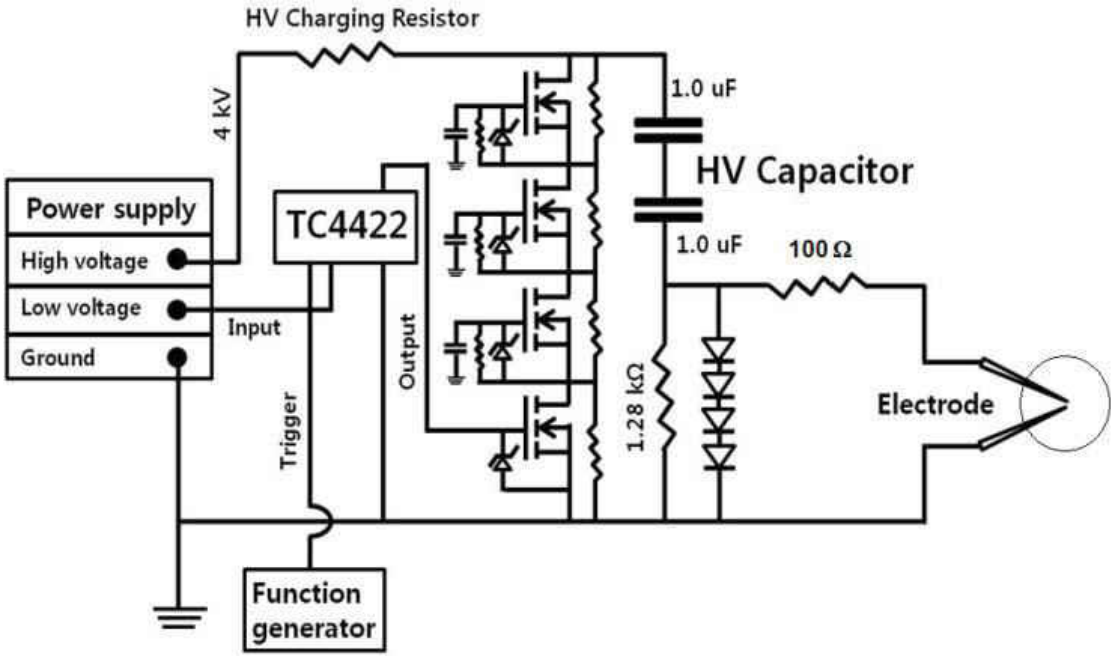

Figure 7. A solid state high voltage generator [11] © 2014 IEEE.

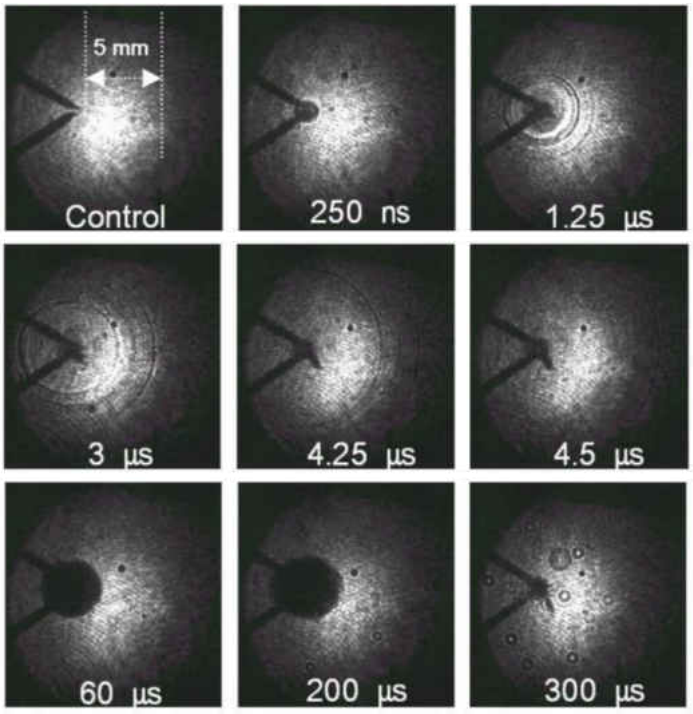

Figure 8. Laser shadow graphs of a 4 kV water discharge creating a shock wave and cavitation bubbles [11] © 2014 IEEE.

CHAPTER 3
PIEZOELECTRICITY

3.1 Piezoelectricity Theory

The Greek word, *piezo*, means to press. The origin of piezoelectricity was in the 1800s when Carolus Linnaeus and Franz Aepinus made the observation that some electric charges can be generated in certain materials when their temperature changes. However, piezoelectricity as a rigorous research field did not exist until the Curie brothers linked the piezoelectricity to the crystalline structure of a material (mineral or ceramic). They found that tension and pressure generate voltage across crystals (direct piezoelectric effect) [18]. The piezoelectric effect was first called by W. Hankel and he postulated the mathematical theory behind the Curie brothers' observations. In 1881, Gabriel Lipmann mathematically deduced the inverse piezoelectric effect via the laws of thermodynamics. In 1917, Pual Langevin and his coworkers introduced a submarine detector using an ultrasonic transducer made of quartz. The basis of their system is to calculate how much time it takes for the sound to echo a submarine so that they can calculate its distance. For ceramics, major historical moments were the discovery of piezoelectricity in potassium dihydrogen phosphate (KDP) family by Busch and Scherrer and the work of Jaffe and his coworkers on lead zirconate titanate (PZT) [19]. These transducers operate according to the polarity of the polar domains inside the transducers. The piezoelectric properties are present in specific dimensions, which create different modes for piezoelectric transducers such as radial, thickness and longitudinal vibration mode, see Figure 9.

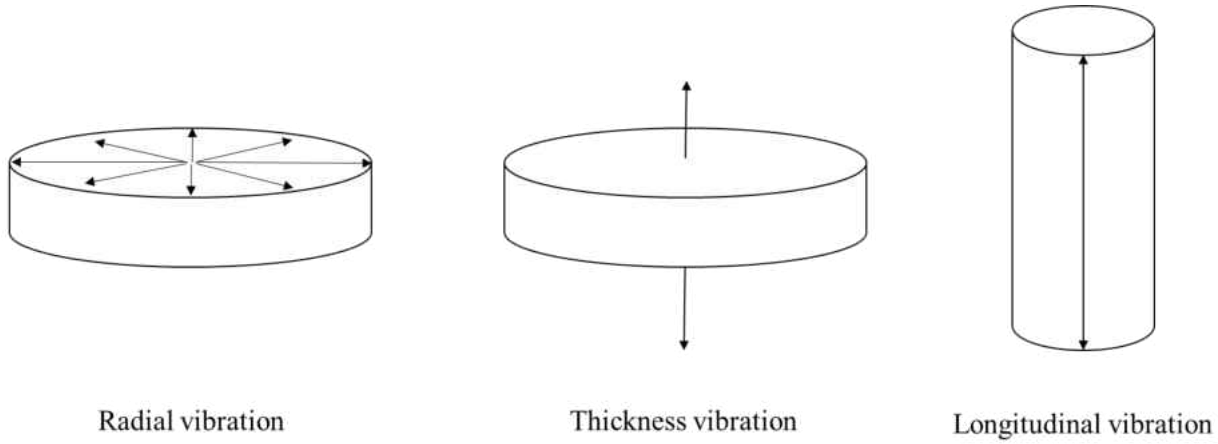

Figure 9. Vibration modes of ceramics.

Piezoelectric materials are used in a variety of applications. They have been in use in microphones, transducers, accelerometers, medical instruments, and power harvesting solutions, etc. Piezoelectric materials are classified as smart materials that can be made into a variety of shapes and geometries [20]. Piezoelectricity is divided into two effects, direct effect and inverse effect. The direct effect is where charges are built up between the surfaces as a capacitor when a piezoelectric material experiences pressure or tension forces. As a result, a potential is established within the material. The inverse piezoelectric effect is that the material produces a mechanical force when an electric field is applied. Essentially, piezoelectric materials are energy storage devices much like capacitors, but they dispense stored energy mechanically by creating a motoring effect that converts the stored electric energy into mechanical energy. Alternatively, they can be viewed as a generator that converts mechanical energy into electrical energy [21]. Such a capability makes the piezoelectric transducer an ideal choice for pressure sensing and acoustic generation.

The coupling of piezoelectric effects includes electrical, mechanical and thermal quantities. Piezoelectricity is considered as a thermodynamic closed system, which includes six parameters:

electric field, mechanical strain, temperature, electric displacement, mechanical stress, and entropy (see Appendix A for more details). The electric field is related to electric displacement by the permittivity of the material, the mechanical strain is related to the stress by the elasticity of the material, and the temperature is related to the entropy by the heat capacity of the material. In general, they can be categorized in three effects:

1. Electromechanical (piezoelectricity)
2. Thermomechanical
3. Electrothermal (pyroelectricity)

Piezoelectric materials are crystalline structures with special properties that makes it piezoelectric. For a single crystal as shown in Figure 10, when an external electric field is applied the crystal begins to stretch its length along the direction of the electric field (motor affect). When an external electric field manipulates the ions (charges), a dipole moment arises between a cation and an anion. That being said, there are many charges within the material and its total dipole moment per unit volume represents its polarization. When a mechanical stress is excreted on a piezoelectric material, the geometry of the crystal structure will change, i.e., ions will separate from the structure. As a result, dipole moments will start to generate a net polarization, thus an electric field will develop that is proportional to the stress applied. This is known as the direct piezoelectric effect (generator effect).

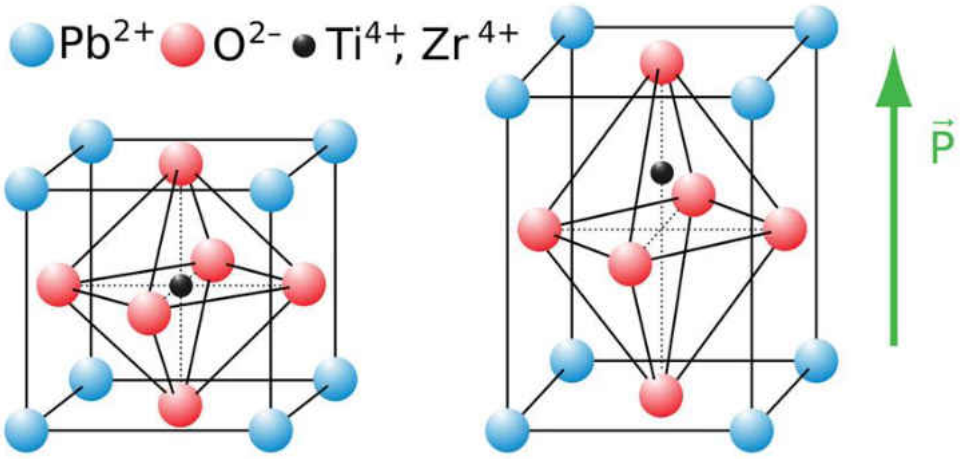

Figure 10. PZT under external polarizing electric field [22].

While energy is converted from electrical to mechanical, some energy will be lost and the electromechanical coupling coefficient is given as the ratio between the converted energy to the input energy. All of the transducers used in this work are thickness vibration mode transducers, and the coefficient for thickness mode is given by the following formula:

$$k_t^2 = \frac{h_{33}^2 \varepsilon_{33}^S}{c_{33}^D} \tag{2}$$

where h_{33} is the piezoelectric field constant, ε_{33}^S is the permittivity at a constant strain (clamped permittivity), and c_{33}^D is the elastic stiffness at constant dielectric displacement [23]. The above expression is derived from thermodynamic principles and the constants with their subscripts are described in Appendix A.

The resonance frequency of a thickness vibration piezoelectric transducer is determined by the piezoelectric frequency constant,

$$N_t = f_p \cdot t \tag{3}$$

where f_p is the parallel frequency and t is the transducer's thickness. The parallel frequency is a function of the density ρ and the elastic stiffness at a constant dielectric displacement c_{33}^D,

$$f_p = \sqrt{\frac{c_{33}^D}{4\rho t^2}} \tag{4}$$

3.2 Equivalent Circuit Models

A common equivalent circuit of a piezoelectric transducers is the Van Dyke model, which is often adopted to simulate electromechanical resonance characteristics of crystal oscillators. The series RLC circuit represents the mechanical damping, mass, and elastic compliance. The series RLC constitutes the mechanical resonance frequency of the piezoelectric transducer and C_0 that is connected in parallel with the RLC represents the capacitance between the conductors' plates of the transducer (Figure 9) [24]. This circuit is only useful if the circuit parameters are constant and independent of the frequency, which is generally the case for a narrow range near the resonance frequency for piezoelectric vibrators.

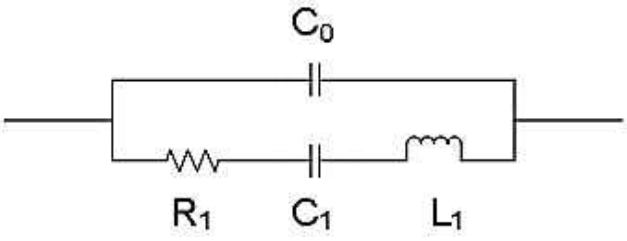

Figure 11. Van Dyke model [24] © 2008 IEEE.

Measuring the impedance for a transducer and finding the minimum and maximum impedances to identify critical frequencies (f_s and f_p) which are the series and parallel frequencies respectively. Once the critical frequencies are determined the piezoelectric constants can be estimated such as the electromechanical coupling coefficient k_t per IEEE standards ANSI/IEEE 176-1987.

$$k_t^2 = \frac{\pi}{2}\frac{f_s}{f_p}\tan[\frac{\pi}{2}\left(1-\frac{f_s}{f_p}\right)] \tag{5}$$

A detailed analysis on this equivalent circuit model is found in IEEE standards 177 [25].

The previous model is for unloaded piezoelectric transducers, meaning that the transducer is not attached to any material that can be considered as a significant source of vibration. To model an attached transducer to some material, more components are added. For the above models, parallel connected series RLC networks are added accounting for the added resonances of the materials that oscillate independently from the transducer [24] (Figure 12).

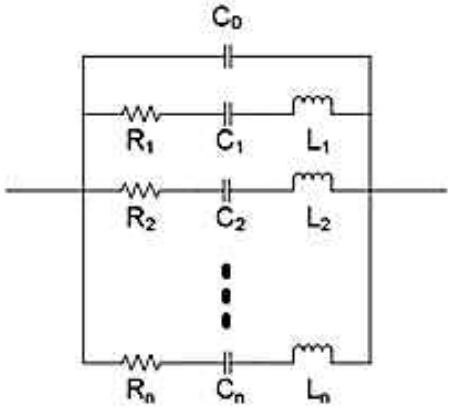

Figure 12. Extended Dyke model [24] © 2008 IEEE.

CHAPTER 4

MEASUREMENT OF PRESSURE

Shock waves can form in air and in liquids. Typically, a measurement of pressure is done by piezoelectric sensors or fiber optic hydrophones. Piezoelectric sensors are widely used and can be used everywhere regardless of the medium. But an environment where shock waves are coupled with high voltage, high frequency disturbance, and piezoelectric transducers can be noisy. A fiber optic transducer then becomes a better option. This is the case for underwater measurements. Through this project a fiber optic hydrophone (ONDA HFO-690) was used.

4.1 Piezoelectric Pressure Sensor

To measure the shock wave pressure in air generated by shock tubes, a piezoelectric pressure sensor can be used. One example is the PCB 113B24 model that is connected to a signal conditioner (PCB 482C) shown in Figure 13. The sensor needs to be bolted to a fixture that holds the sensing end of the sensor facing the direction of the shock. Once the shock reaches the sensor, the quartz plates inside the housing generate voltage that is proportional to the shock pressure. The voltage is then amplified by an integrated circuit inside the housing, see Figure 14 for the internal components of the sensor. The signal is then sent to the signal conditioner that filters noises before the pressure data acquisition. The sensitivity of this particular system is 0.725 mV/kPa and the sensor is capable of measuring pressure gradients up to 13.8 MPa [26].

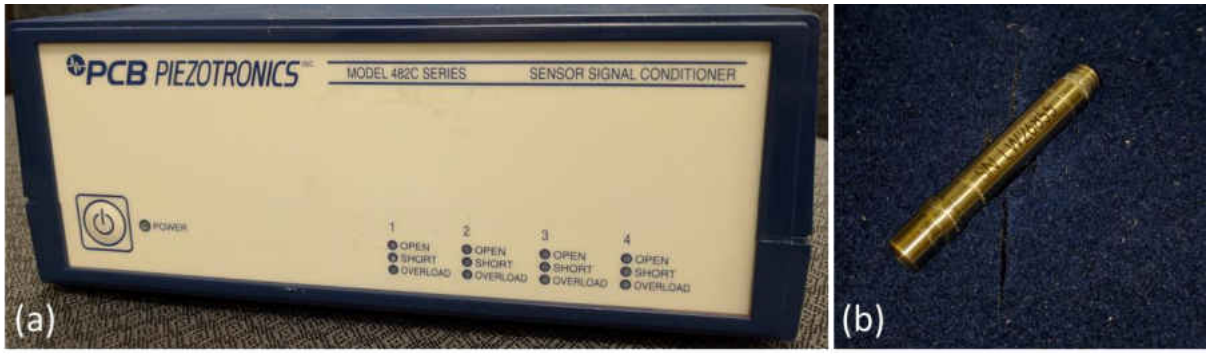

Figure 13. Photo of (a) a signal conditioner and (b) a piezoelectric pressure sensor.

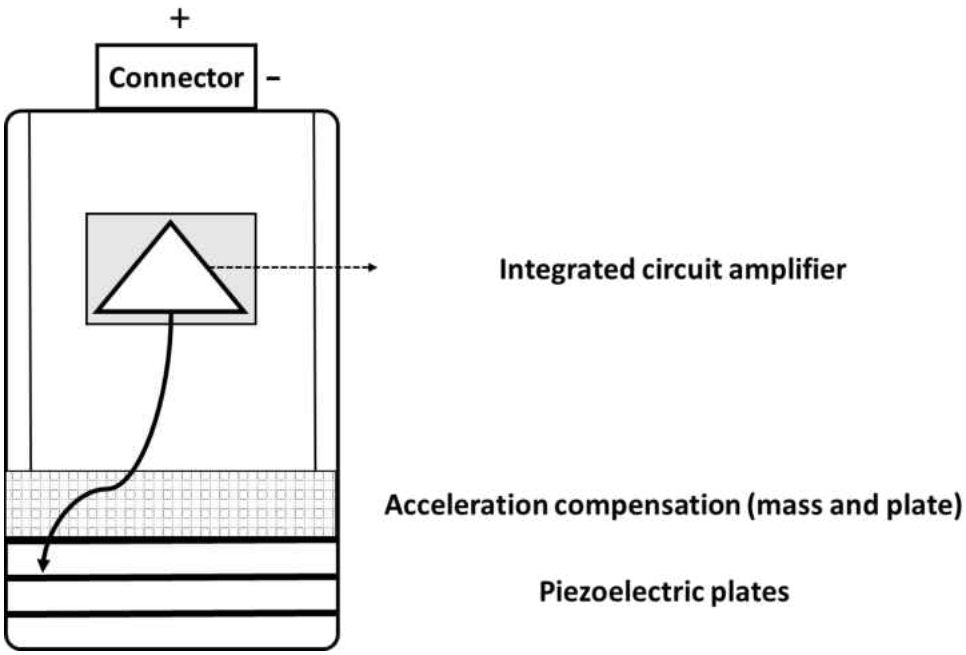

Figure 14. The internal components of PCB 113B24.

4.2 Fiber Optic Hydrophone

The fiber optic hydrophone used (ONDA HFO-690) is shown in Figure 15, which is comprised of a digital controller and a fiber optic cable. The controller houses a 690 nm laser diode whose light is propagated in a multimode fiber optic cable that has a diameter of 150 µm. The fiber tip is submerged in water and the pressure changes are sensed by the tip, which modifies the dielectric property of the fiber and results in the phase change of the laser light. The process of the measurement of pressure is shown in Figure 16 where a pressure generation device (a piezoelectric disc) is mounted at the bottom of a water tank and the fiber is submerged in water. Once the pressure change occurs at the tip of the fiber, the controller converts the change of pressure to a change in voltage. The output from the controller is sent to a digital oscilloscope (Tektronix TDS3054C). The data are then recorded and processed to obtain the actual pressure using the calibration factor.

Figure 15. ONDA HFO-690 fiber optic hydrophone (pressure sensor).

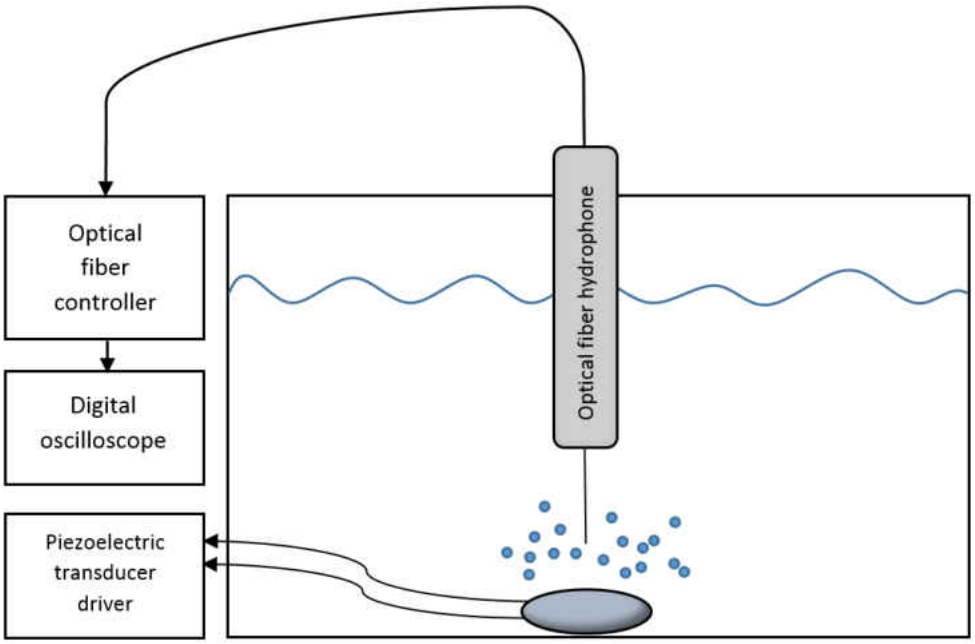

Figure 16. Pressure measurement using fiber optic hydrophone.

4.3 Preparation and Calibration

Generally, all optic devices are sensitive to contaminants such as dust. The first step in preparing this device is to clean the optic connection between the fiber and the controller. A 0.016 inch stripping tool can be used to strip out 45 mm of the protective jacket of the fiber. For a smaller stripping, a 0.006 inch stripper is used to strip out approximately 25 mm of the cladding layer. Finally, the end of the fiber has to be cut precisely with a cleaver tool as shown in Figure 17. Now that the fiber is prepared, the device has to be calibrated. To understand the calibration, the principle of the optic fiber hydrophone will be explained next.

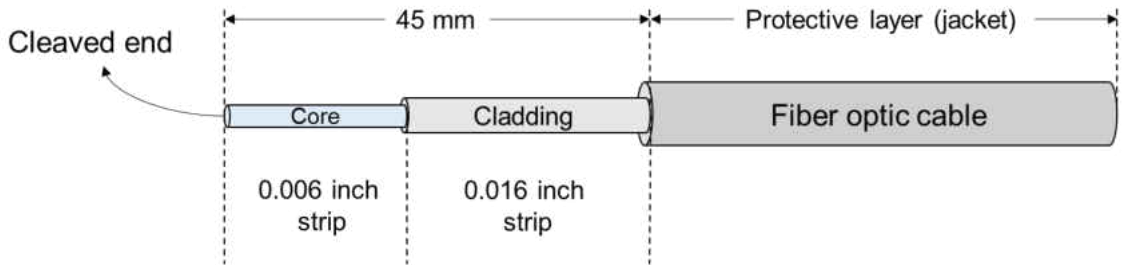

Figure 17. The preparation of using fiber optic hydrophone.

For a light that runs across a different medium, the Fresnel's formula for the reflection coefficient is:

$$R(T,p) = \frac{\left(n_c - n_w(T,p)\right)^2}{\left(n_c + n_w(T,p)\right)^2} \tag{6}$$

where n_c is the refractive index of silica glass of the fiber's core material which is 1.45552 at 690 nm and n_w is the refractive index of water which is about 1.33. Water, in this case, experiences a change of dielectric property, i.e., the refractive index, due to the change of pressure and temperature. The hydrophone is equipped with a photodetector that produces a voltage that is proportional to the reflected power or reflection coefficient:

$$\Delta V = K_{rf}\Delta R \tag{7}$$

where K_{rf} is a constant that is dependent on the power of the laser, the sensitivity of the photodetector, and the efficiency of light transmission to the fiber. The K_{rf} constant is obtained by performing a series of calibrations that the manufacturer refers to as a DC offset calibration and a sensitivity calibration. To perform the DC offset calibration, the fiber has to be submerged in a

special medium that has a matching refractive index to the fiber, which provides a reference voltage V_0 at zero reflectance ($R = 0$) as the following:

$$V - V_0 = K_{rf} R(T, p) \tag{8}$$

After the DC offset calibration is performed, the fiber has to be submerged in water to do the sensitivity calibration. The water's temperature has to be measured externally and entered to the device by its touch screen. Since the water's pressure is assumed to atmospheric (p =101 kPa), a solution can be found for the K_{rf} constant. Since V_0 is measured and $R(T, p)$ is known from water properties [27] and [28], Equation (4) can be solved to obtain K_{rf} constant. The controller provides a linear approximation factor, sss, small signal sensitivity [23], so the voltage can be converted to meaningful pressure in MPa:

$$\Delta p(t) = sss.\Delta V(t) \tag{9}$$

The calibration numbers should be within the manufacturer's specification. That is to say, the DC offset should be in the range of 0.1 V to 0.5 V and the sss should be between 5 mV/MPa and 8 mV/MPa [29].

CHAPTER 5

PIEZOELECTRIC TRANSDUCER DEVICES

5.1 Power Amplifier

The driver of a piezoelectric transducer needs to produce bipolar voltages that last a couple of cycles or a prolonged time. The production of continuous acoustic pressure however is not considered here because significant heat may generate and contaminate the biological results. The bipolar voltage can be produced by amplifying low-voltage sinusoidal wave. A function generator (Agilent N9310A) was used to modulate a sinusoidal signal. It was connected to a broadband amplifier (Kalmus 706FC-CE). The output of the amplifier was connected to a resistor to match its impedance. The amplitude of the final output was controlled by the function generator's power controlled. For example, when the function generator's power is set at -4 dBm, the amplifier's output will be ~ 15 V.

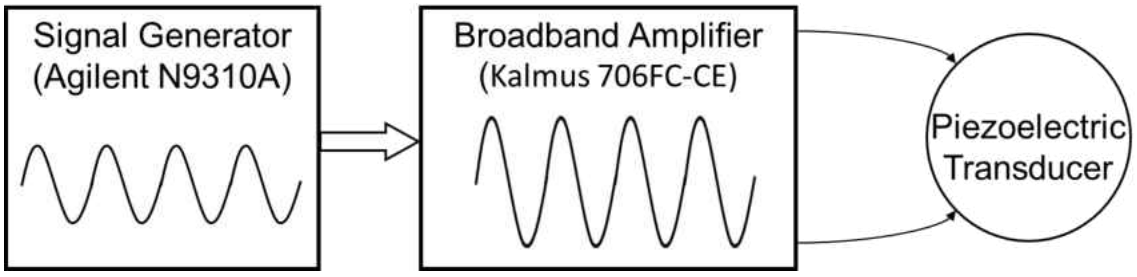

Figure 18. A simple testing setup that has an off-the-shelf broadband amplifier.

5.2 Push-Pull Circuit

The push-pull circuit shown in Figure 19 uses two power MOSFETs, an N-channel MOSFET (Vishay IRFP450), and a P-channel MOSFET (IXYS IXTH16P60P). To drive these MOSFETs, a signal generator (Agilent N9310A) and a wideband RF amplifier (Kalmus 706FCCE) were used. The signal was fed to the amplifier at -4 dBm, from which the amplified output was fed to the MOSFET's driver circuit. This RF signal was coupled through a wideband transformer (Pulse PE-65612NL) which was connected to the gates of the MOSFETs. The output pulse duration was controlled by the signal generator and set to 600 ms. Two 1 mF capacitors (C1 and C2 in Figure 19) were used in the circuit and they were charged by two DC power supplies (Bertan 210-05R and Bertan 210-03R) running at the opposite polarity but with the same voltage amplitude (100 V). The N-channel MOSFET is turned on when the driving waveform is positive, allowing C1 to discharge to the piezoceramic transducer. The P-channel MOSFET is turned on when the driving waveform is negative, allowing C2 to discharge to the piezoceramic transducer. The output of this circuit is shown in Figure 20 and Figure 21.

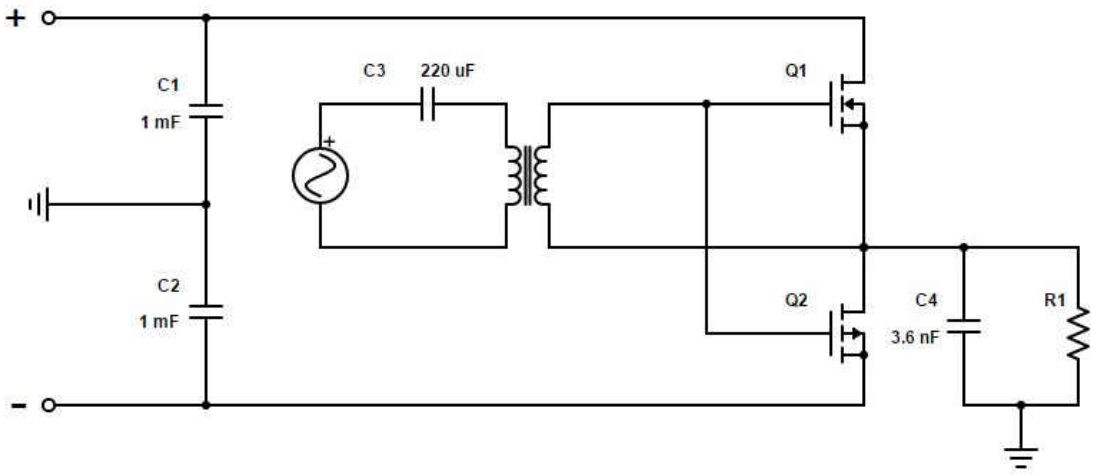

Figure 19. The Push-Pull circuit.

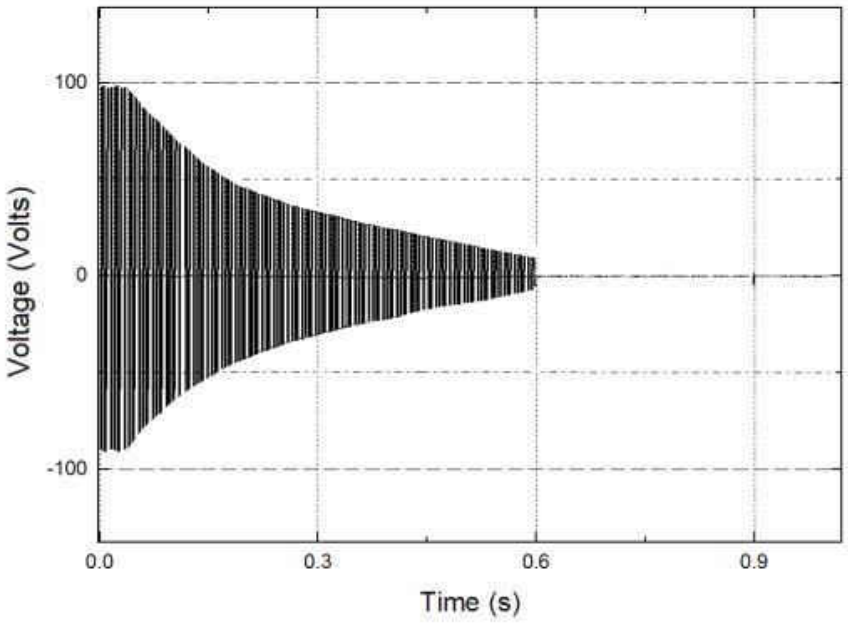

Figure 20. The voltage that delivers to the load.

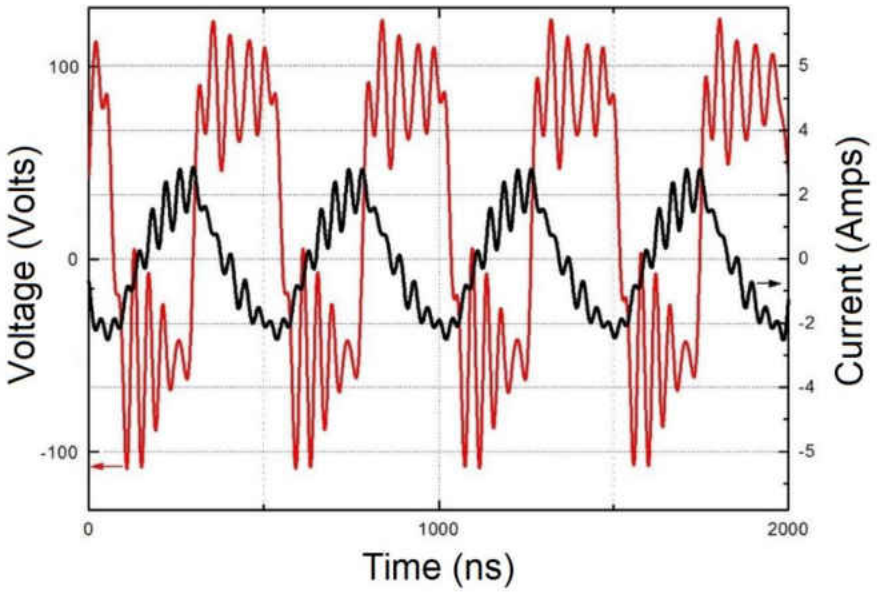

Figure 21. The voltage and current have a period of 2.1 MHz.

5.3 Self-Resonance Circuit

Another piezoelectric driver circuit is a self-resonance circuit. It is commonly used in water atomizers, as shown in Figure 22. The circuit drives the transducer at the resonance frequency of 2.1 MHz. The circuit takes the power from the standard household voltage (~120 Vrms) which is stepped down by a transformer to ~ 28 Vrms before rectification. A relay (Tyco CNS-35-72) is connected to the primary of the transformer to control the ON time for the circuit (up to 10 seconds of ON time). An oscillator circuit consisting of two serial inductors (L1 and L3) in parallel with the capacitor C3 determines the oscillation frequency. When Q2 is turned on and C3, L1, and L3 are charged, Q1 turns on. The voltage feedback of L1 to the base of Q1 through C4, calls for more current for the fast charging of L1. The oscillation rises from the discharging and charging between C3 and L1, switching Q1 on and off. C5 and C6 provide AC short circuit for the transducer and the cycle is repeated by the turning on of Q1. The output voltage (at the transducer) is similar to Figure 23. The circuit produces approximately 70 V (peak to peak voltage) and approximately 5 A (peak to peak current). The phase difference was calculated to be about 24° (Figure 24). The average output power is 21.20 Watts. Since the piezoelectric transducer has an electromechanical coupling coefficient k_t = 0.46, the mechanical average power is 9.76 Watts.

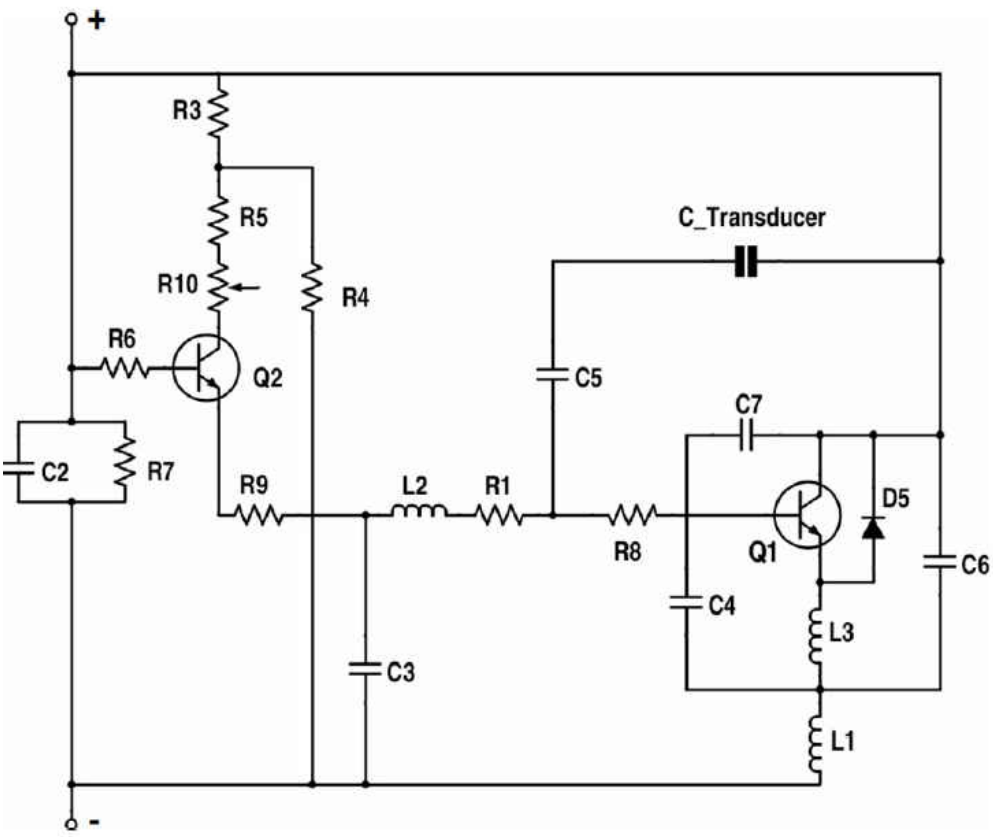

Figure 22. A self-resonance circuit used in an atomizer [30].

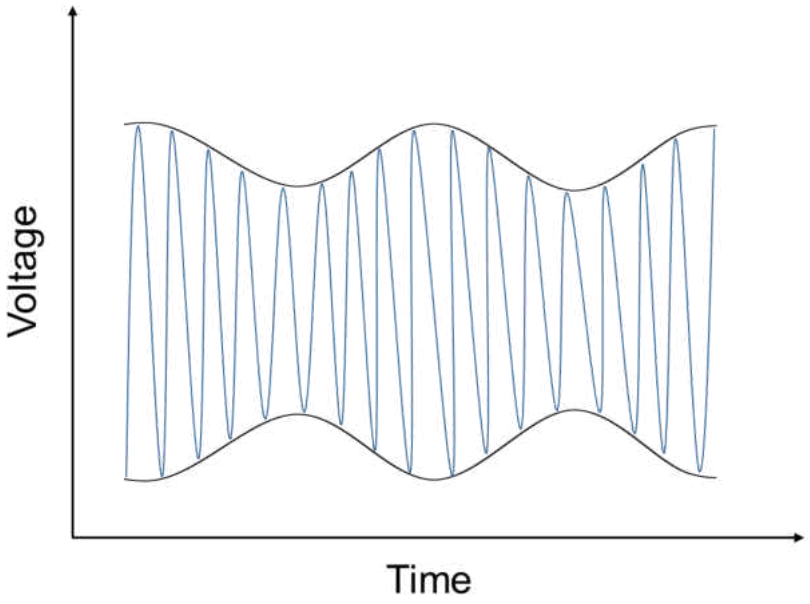

Figure 23. The voltage in the self-resonance circuit.

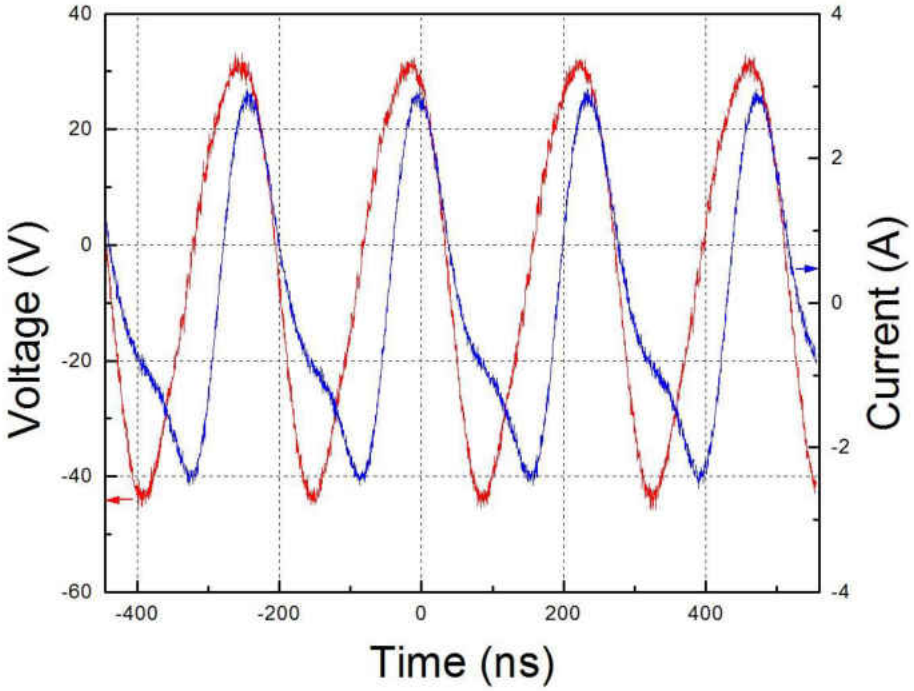

Figure 24. The voltage and current in the self-resonance circuit.

CHAPTER 6

PIEZOELECTRIC MICROBUBBLE GENERATOR

Piezoelectric transducers produce acoustic pressure when an oscillating electric field is applied. Piezoelectric transducers are available in a variety of sizes, shapes, and frequencies. Using parabolic transducers (referred to as spherical by the manufacturer), the acoustic waves can be focused. The size is a key feature that enables the design of a system compact enough to be used under a microscope. In this section, the design of the system, the final design, and results will be discussed in detail.

6.1 Transducers

Several piezoelectric transducers acquired from *STEMiNC* and *RadioShack* were tested for cavitation production in the tap water. The transducers were put in a transparent beaker and driven by the power amplifier described in Section 5.1. The first transducer in the test was a piezoelectric transducer from RadioShack (2730073). It was driven at ~ 18 V at frequencies from 1.5 KHz to 3 KHz. The piezoelectric transducer did not produce any bubbles. Next, four other transducers from STEMiNC were tested. The first two transducers were: 12 × 0.6 mm flat disc (SMD12T06R412WL) and 13.5 × 1.2 mm flat ring transducer with a ring 7 mm in diameter (SMR1357T12R412WL). They were driven at the resonance frequency of 3.4 MHz and 1.7 MHz respectively. These two transducers did not produce any bubbles either. It was speculated that the acoustic power from these transducers wasn't high enough as they are ring-shaped. So the focus was turned to two other transducers, a 19 × 1 mm flat disc (SMD19T1112S) and a 20 × 1 mm spherical disc (SMSF20C30F21, the radius of curvature: 30 mm) (Figure 25) in which bubbles were observed. To observe the bubbles better, a laser was used to enhance the contrast of bubbles

and the background water. The laser of the fiber optic hydrophone was shined at the piezoelectric transducers and the setup is drawn in Figure 26. These two transducers produced large number of bubbles as shown in Figure 27. These transducers were then chosen for bubble generation under the microscope.

Figure 25. Piezoelectric transducers, spherical disc (right) and flat disc (left).

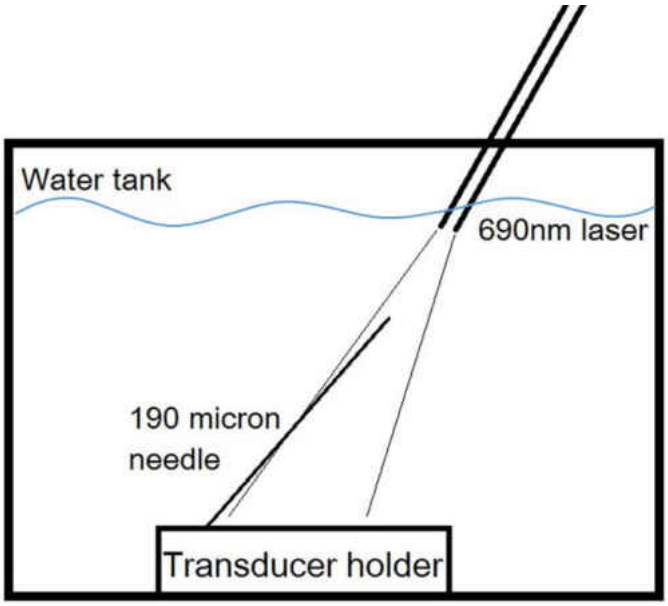

Figure 26. The experimental setup used for capturing bubbles.

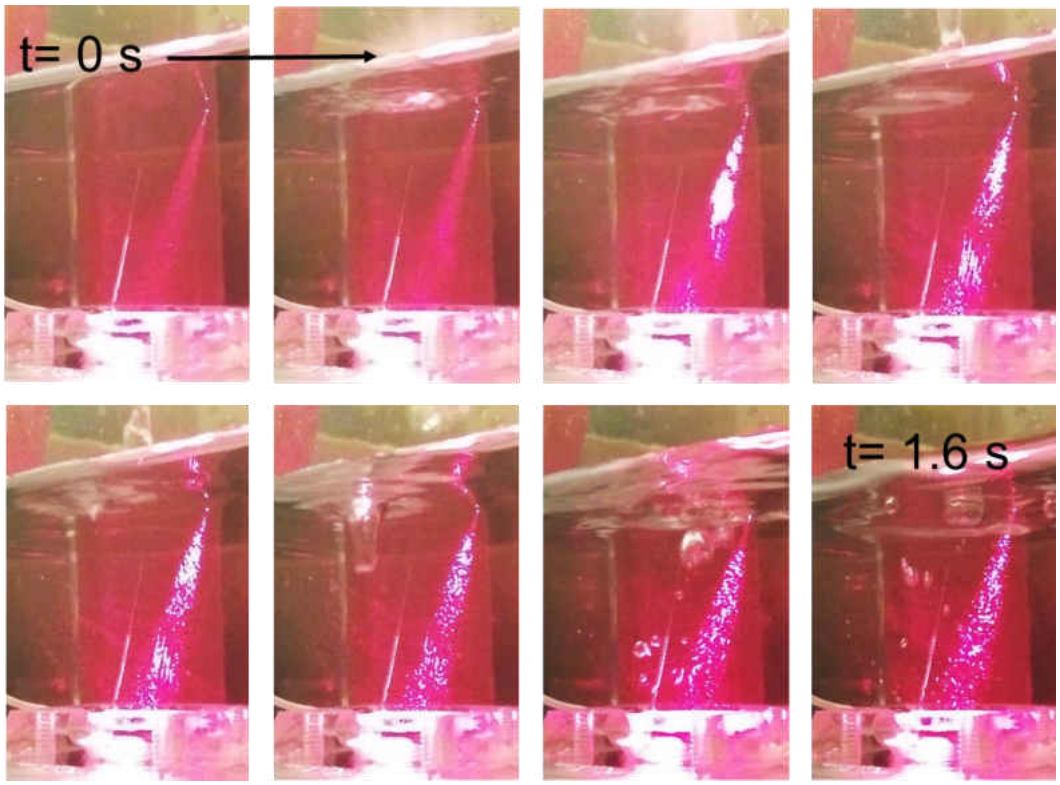

Figure 27. Bubble production in a 1.6 s span.

In an effort to increase the generation of bubbles, the transducers shown in Figure 25 were stacked with 3M double sided tape inserted in between (Figure 28). The transducers were electrically connected in parallel and driven by the push-pull circuit shown in Figure 19. The amount of bubbles did not seem to increase significantly. Thus, this technique was discarded.

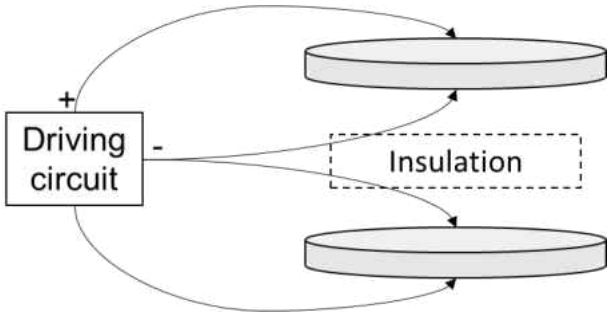

Figure 28. Stacking transducers.

6.2 Chamber Design

Several configurations that included a water chamber and a transducer were designed and constructed to in order to adapt to an upright microscope (Olympus BX51). The chamber was used to contain cell medium and also provides an anchoring location for cover slips on which biological cells are cultured.

6.2.1 Transducer with Aperture

The first configuration was to arrange the transducer to face the cover slip so the pressure waves and bubbles can directly hit the cover slip. Meanwhile, the transducer was drilled in the center so that light from the microscope can go through and reach the cells on the coverslip. This approach turned out to be problematic for the following reasons:

1. the transducer creates a water jet, which pushes the cover slip over. To avoid the jet formation, a deep water chamber must be used.
2. the chamber is difficult to build and difficult to handle as the distance of the chamber to the microscope objective needs to be short for high magnification.
3. when a shallow chamber (12 mm tall) was used, there were no bubbles observed.

So for these reasons, this approach was abandoned.

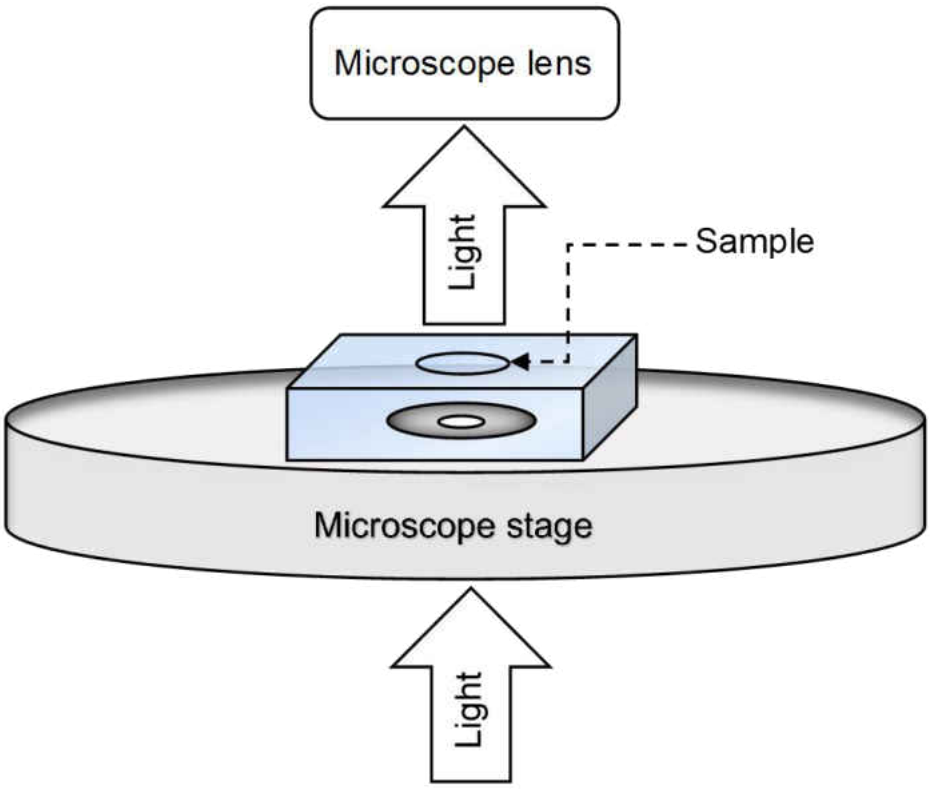

Figure 29. Transducer with an aperture

6.2.2 Two Transducers at an Angle

In the previous experiments, the volume of water was very low. It was thought that if more water is filled in, more bubbles should be produced. Two transducers were then connected in parallel and mounted at an angle as shown in Figure 30. Still, no bubbles were observed. But the conclusion was made that there needs to be a critical length for bubbles to generate.

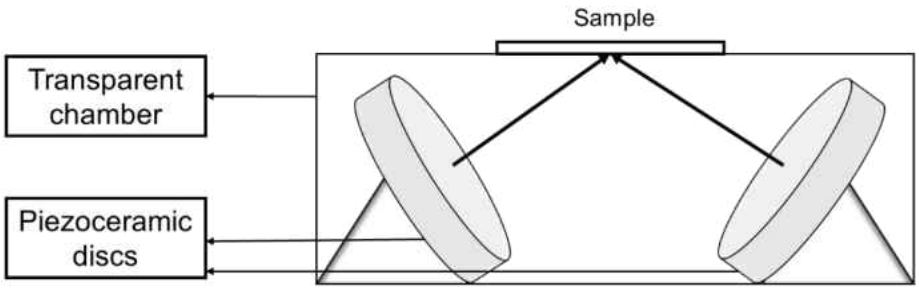

Figure 30. Two transducers combine the pressure at the sample location.

6.2.3 Transducer Mounted on the Side

Since the goal was to produce energetic bubbles but not necessarily acoustic pressure, as the previous study in [7] showed that most damage was done by the bubbles, a decision was made to mount the transducer sideways and to place the cover slip perpendicular to the axis of the transducer. Doing so will not exert pressure directly to the biological sample. Instead, the bubbles will rise and reach the sample because of buoyancy. To produce the bubbles, the transducer needs to be powered for at least 2-3 seconds. But even for this short period, it was observed that the acrylic chamber wall that faces the transducer was heated and melted. This was due to the transition of low impedance to high impedance between the water and the chamber's wall (sonic heating). As acrylic has a melting point of ~ 160 ˚C and glass has a much higher melting point of ~ 1400 ˚C, glass was chosen to make the chamber.

Multiple chambers were constructed and tested under the microscope. The goal was to be able to adept a 40X lens. It was apparent that the chamber needs to be short in height so the object lens won't be obstructed. The two transducers shown in Figure 25 were tested. The flat transducer was found to produce more bubbles than the parabolic one, so it was chosen. In order to shorten the height of the chamber, part of the transducer had to be exposed outside the water, which created

overheating of the transducer. This was particularly problematic if the transducer was continuously powered. As a result, Q1 can be fried (Figure 22). To solve the problem, a relay was added to the circuit with a maximum operation time of 10 s. Moreover, the transducer was trimmed down so that no extra area was exposed to air. The final dimensions of the chamber were designed to be 12 mm high, 25 mm wide, and 78 mm long. Glass sheets 1 mm thick were used to construct the chamber (Figure 31 and Figure 32). The chamber contains a glass lid with a designated coverslip anchor with ample room for placing and removing the coverslip. The chamber was able to fit nicely on the microscope for the 40 X object lens.

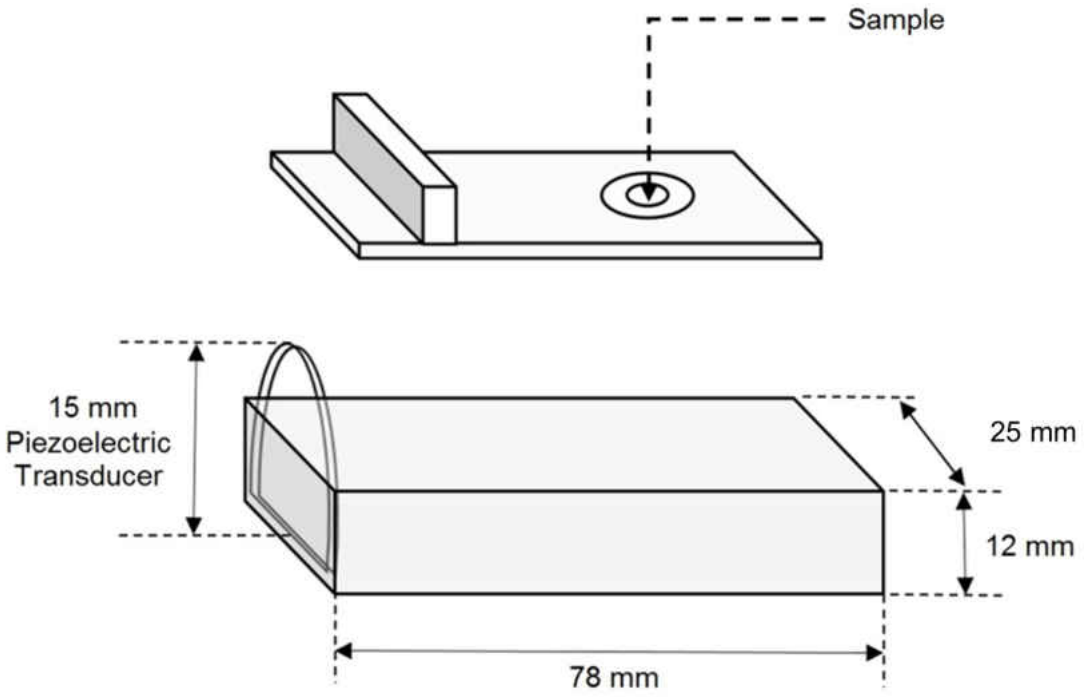

Figure 31. A bubble chamber that has a piezoelectric transducer placed sideway.

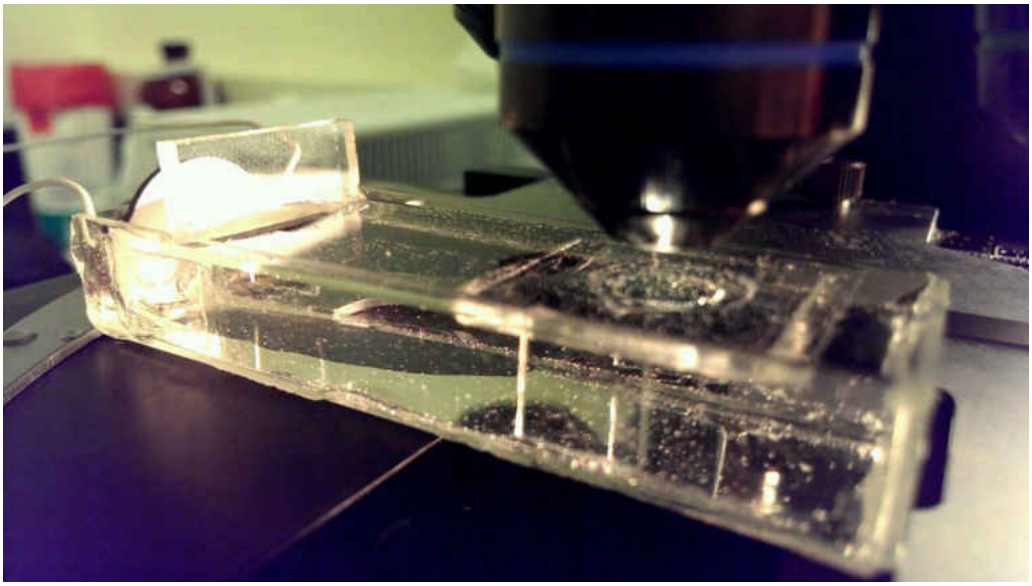

Figure 32. Final chamber fabricated with 1 mm thick glass sheets was placed under a 40X objective lens.

6.3 Final Package

The system was packaged in a plastic box that houses the circuit and is powered by a regular 120V AC from a wall receptacle. The box has an ON/OFF switch and a duration control knob (up to 10 seconds). From the output ports, two electric wires can connect the driver to the piezoelectric transducer that is housed inside the glass chamber.

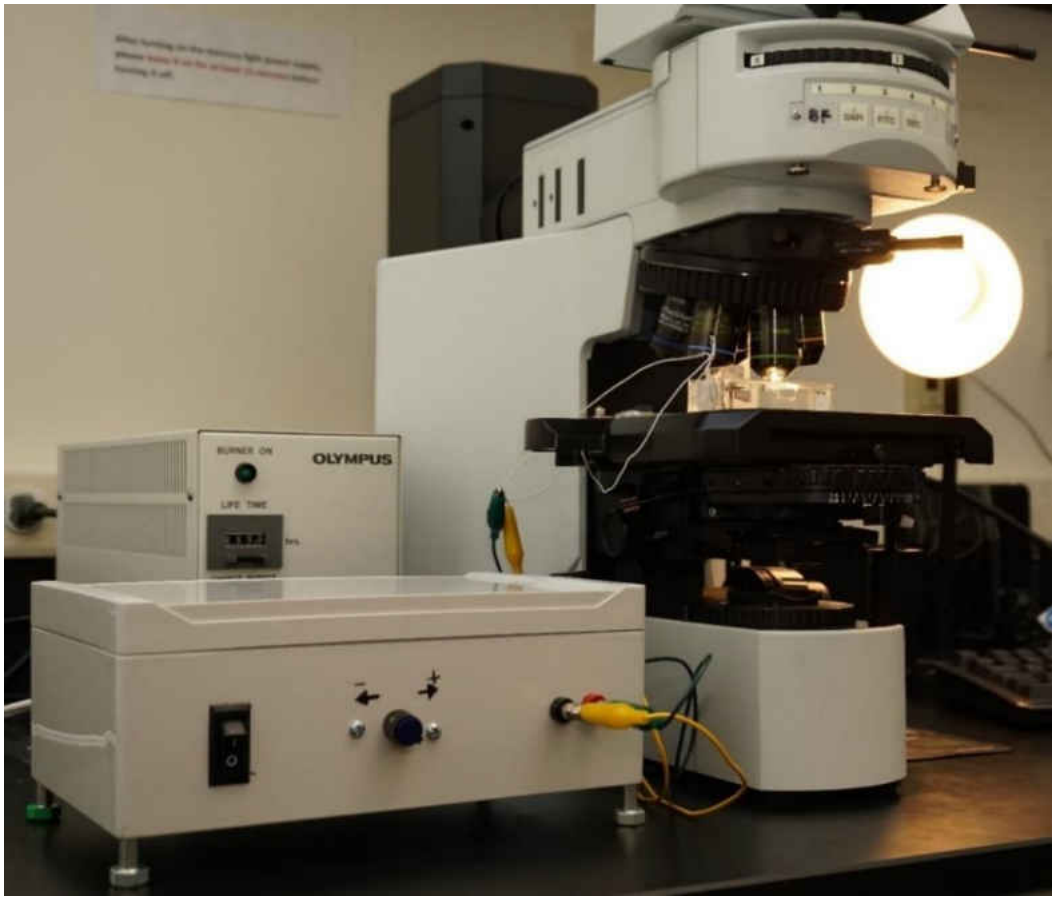

Figure 33. The whole setup of the bubble generator, which includes the driver, the chamber, and the microscope.

CHAPTER 7

EXPERIMENTAL RESULTS

7.1 Pressure Analysis

Pressure data were collected for both parabolic and flat piezoelectric transducers using a fiber optic pressure transducer (ONDA HFO-690). The optical fiber was submerged in water and the fiber tip was directed to the piezoelectric transducer. The fiber was mounted on a 3-D maneuver stage allowing for 1 mm precision. The pressure signal was amplified by the optical fiber controller and further shown on a digital oscilloscope (Tektronix TDS3054C) (Figure 34). Pressure was measured for the two chosen transducers driven by the push-pull circuit and the self-resonance circuit.

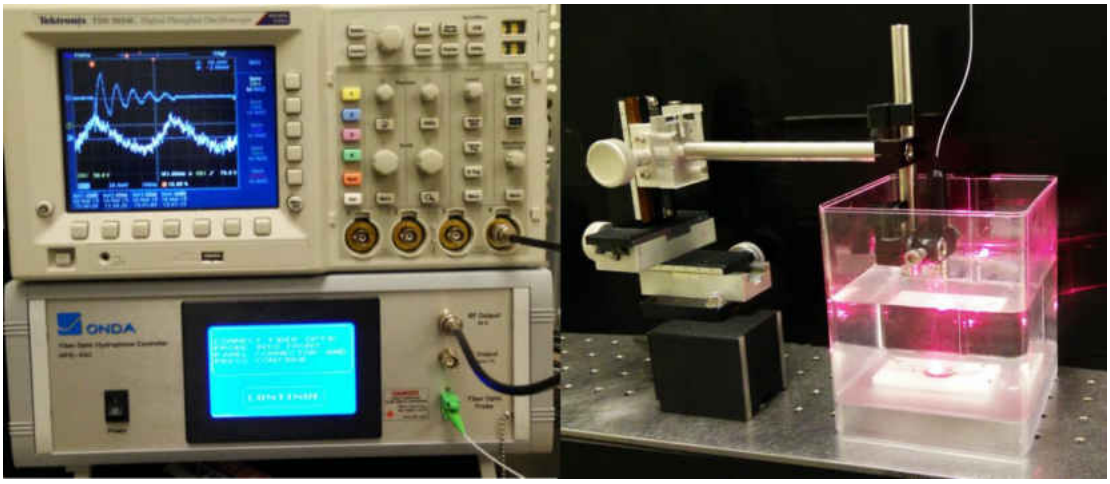

Figure 34. The setup for measuring pressure. Left: the controller for the hydrophone and the oscilloscope. Right: a water tank and a 3 axis maneuver stage that holds the fiber.

7.1.1. Push-Pull Driven Transducers

The push-pull converter (Section 5.2) was turned on for 600 ms. When the pressure was measured, the onset of the pressure was not always the same. The pressure wave sometimes could start from a positive pressure or otherwise a negative pressure. (Figure 35). Even when the transducer was turned on for a different duration, the starting pressure could be different. A probability graph was created to count for the frequency of the positive onset when we varied the duration of the pressure. After the pressure onset, the pressure wave seems consistent in all different operations in Figure 36. However, the frequency of the waves doesn't appear to equal to the frequency that was used to drive the transducer, because the transducer was mounted to a stationary object (loaded) that limited the frequency of the vibrations.

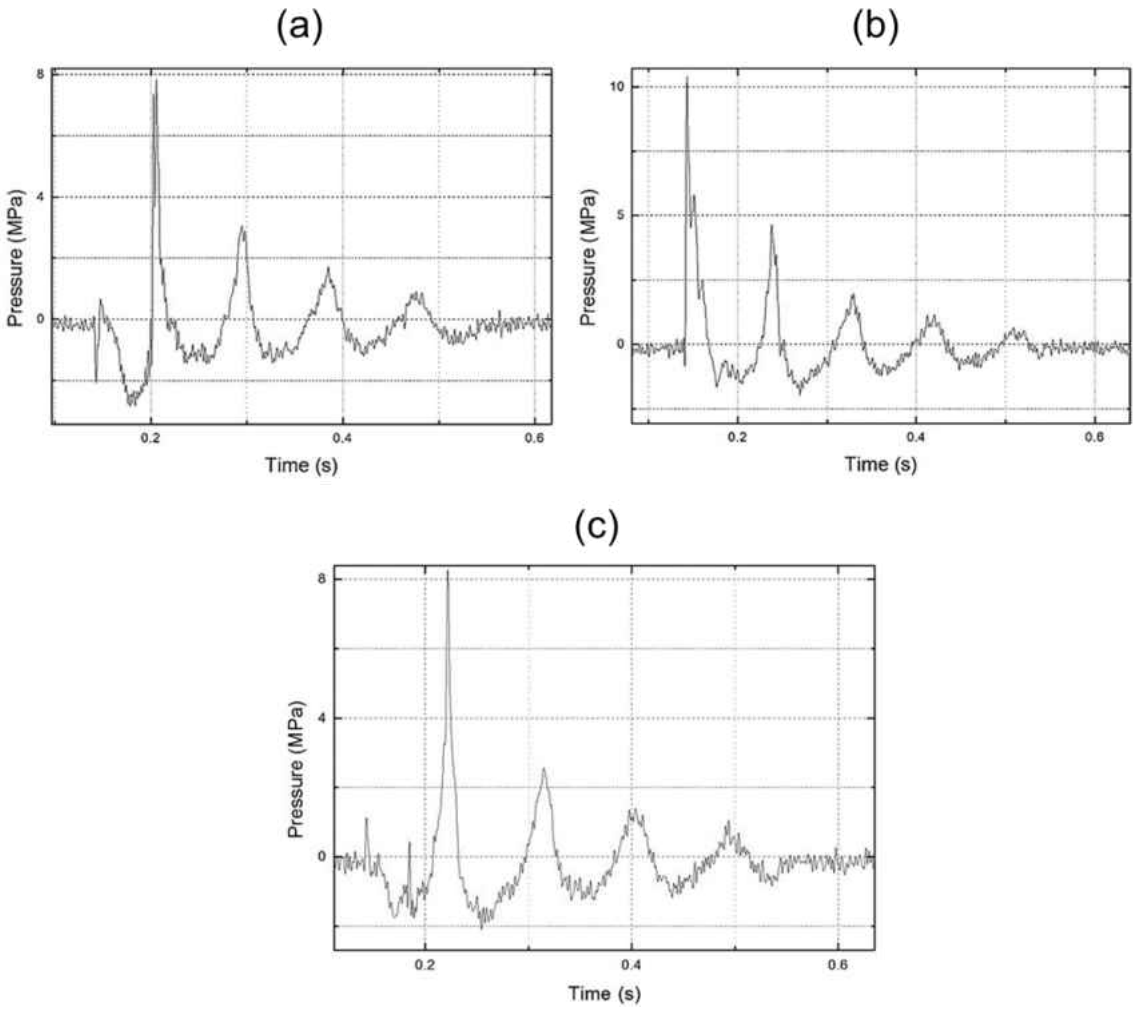

Figure 35. Pressure waves generated by the spherical transducer at its focal point.

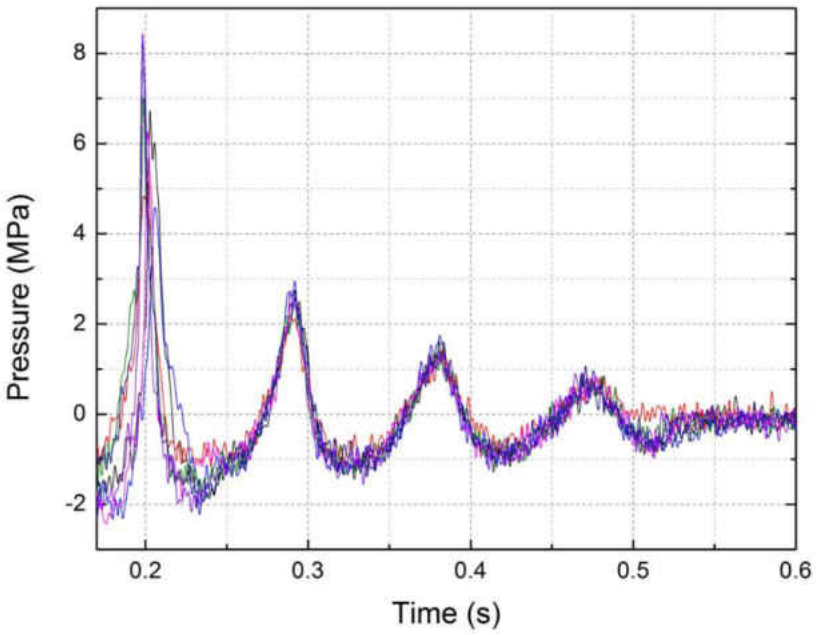

Figure 36. Pressure waves can be plotted in a synchronous way that shows fairly consistent peaks for a spherical transducer. The onsets of the pressure waves are not shown.

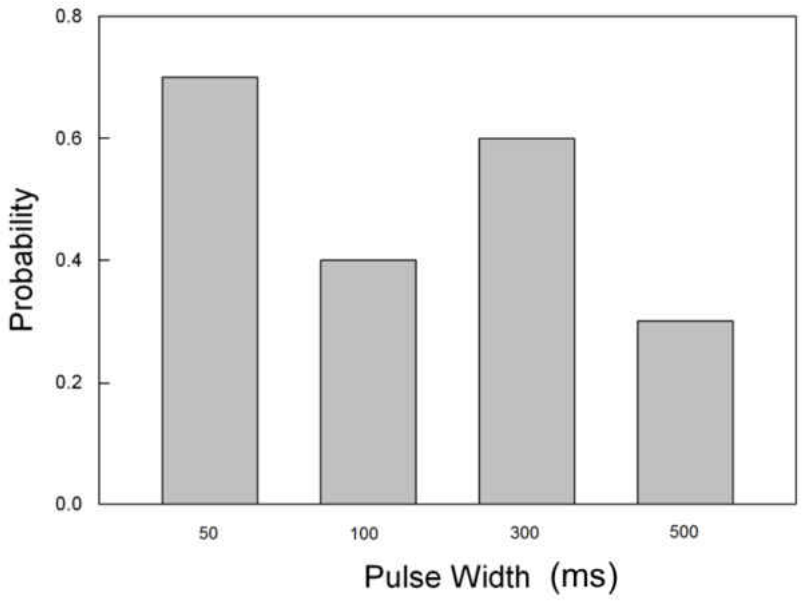

Figure 37. The probability of positive onset versus pulse width.

The flat transducer produced the peak pressure of approximate 2 MPa at 9 mm. The peak pressure decays as the distance increases but becomes stable 12 mm to 20 mm (Figure 38). On the other hand, the spherical transducer shows a peak pressure ~9 MP at 30 mm, which is predicted by the curvature (30 mm) of the transducer (Figure 39). Meanwhile, the pressure was measured laterally and the peak pressure was found on the axis (Figure 40). The pressure was also measured for the transducer with the aperture in a similar manner (Figure 41 and Figure 42).

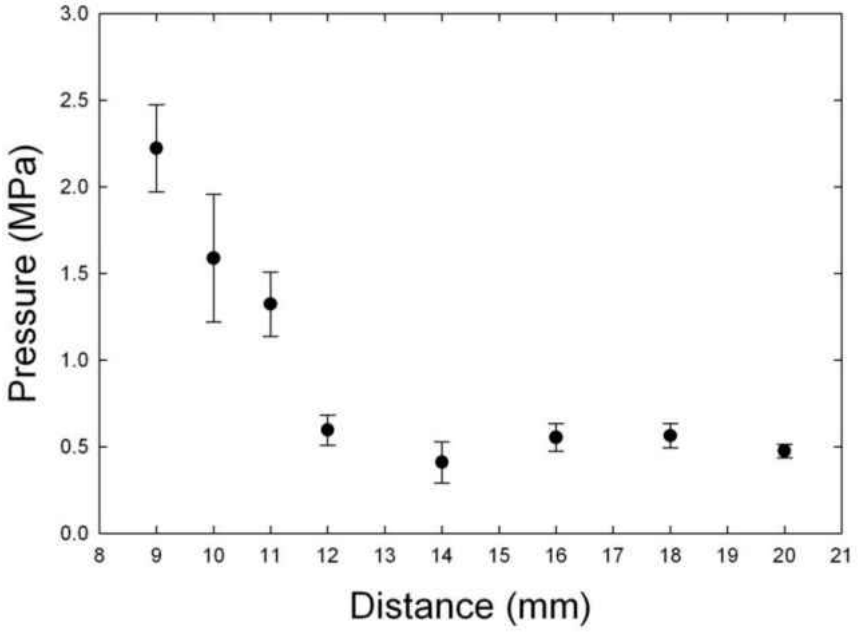

Figure 38. Vertical pressure distribution – flat transducer.

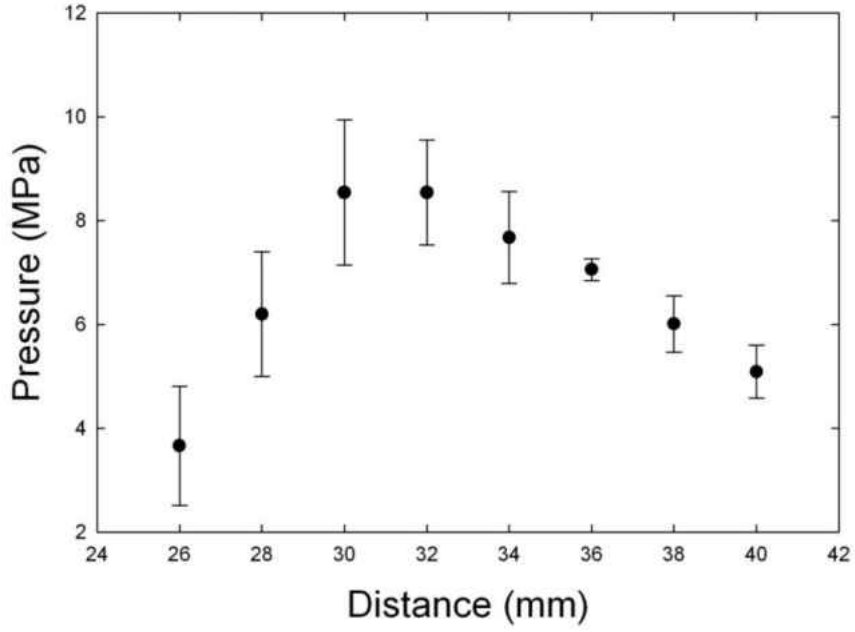

Figure 39. Vertical pressure distribution – spherical transducer.

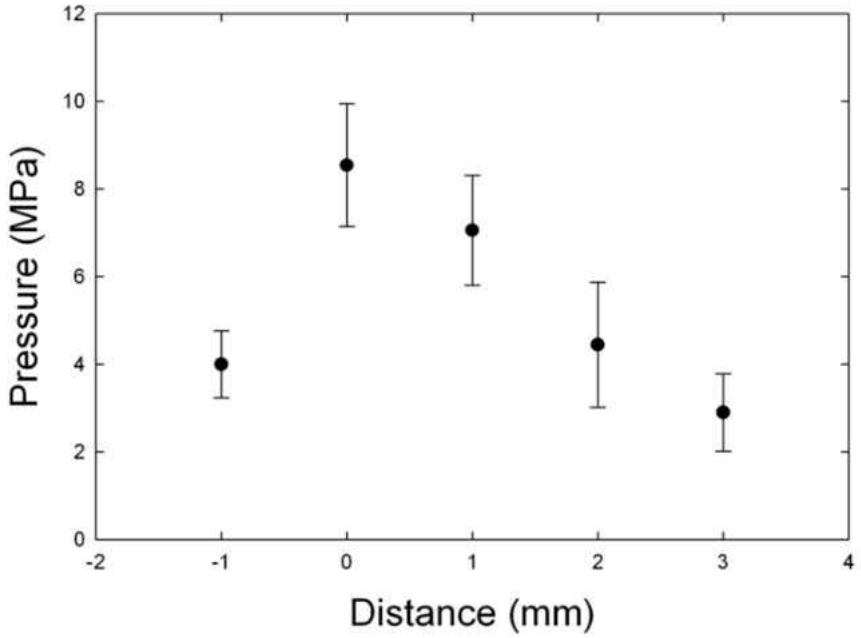

Figure 40. Lateral pressure distribution – spherical transducer.

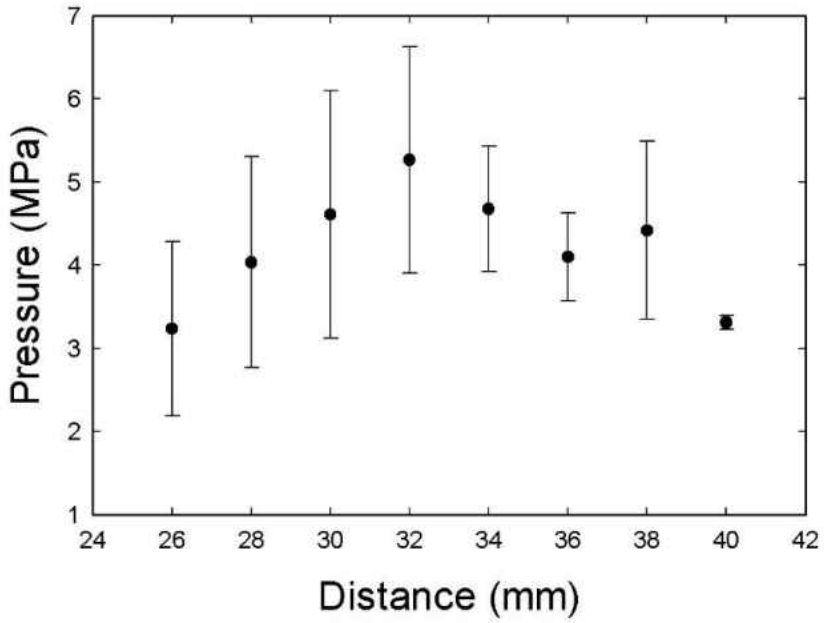

Figure 41. Vertical pressure distribution – spherical transducer with an aperture.

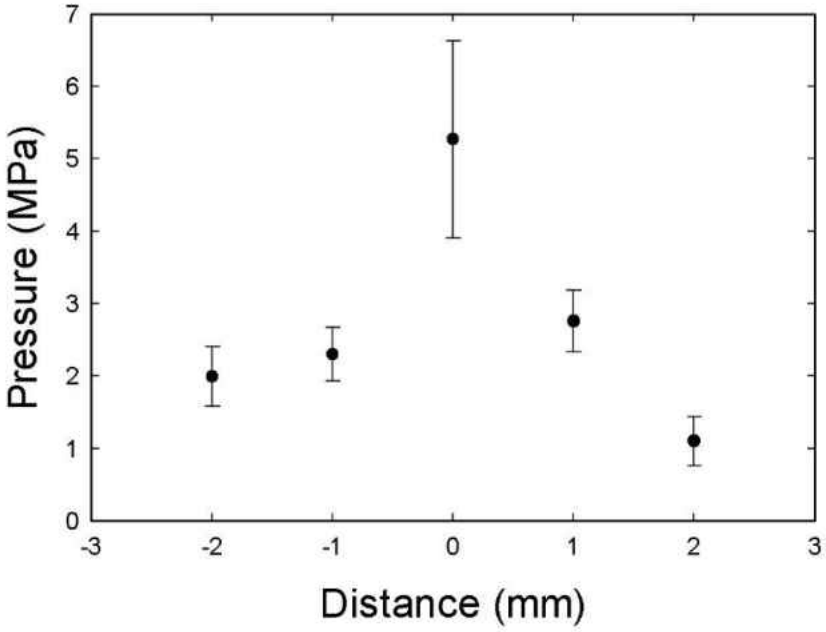

Figure 42. Lateral pressure distribution – spherical transducer with an aperture.

7.1.2 Transducers Driven by Self-Resonance Driver

The same pressure measurements were performed but the transducers were free loaded in the water tank. The self-resonance driver energized the transducer at 2.1 MHz and the frequency of the pressure wave was measured approximately 2 MHz (Figure 43), which matches the theoretical frequency, f, given by the material's frequency constant:

$$f = (N_t = 2050\ Hz.m) \div (thickness = 1\ mm) = 2.05\ MHz \qquad (10)$$

The peak of the pressure is 8 MPa and stays relatively constant at each cycle. For flat transducer, the same frequency was observed but the amplitude was 1 MPa. The spatial distributions of the pressure for both transducers are plotted in Figure 46. Again, the curved transducer shows a nice focused pressure distribution, whereas the flat transducer produces a stable pressure distribution throughout the measurement range.

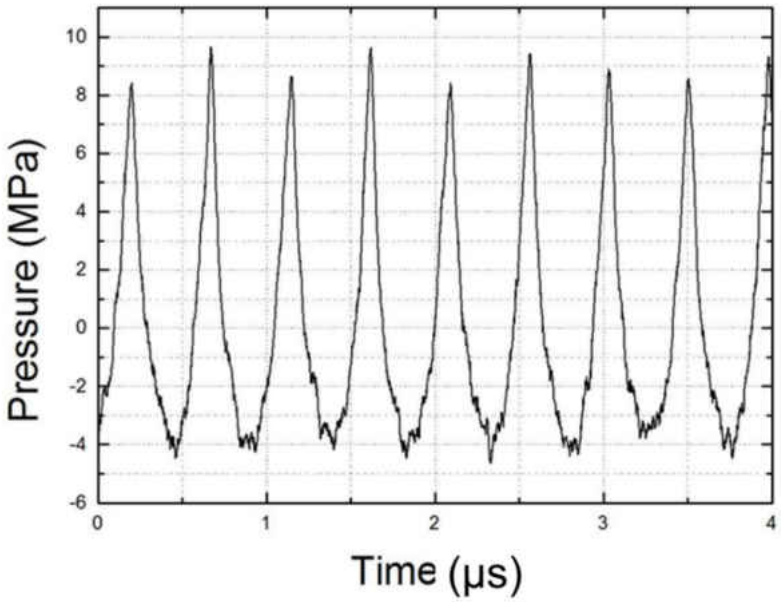

Figure 43. The pressure at the focal distance of 30 mm produced by the spherical transducer driven by the self-resonance circuit.

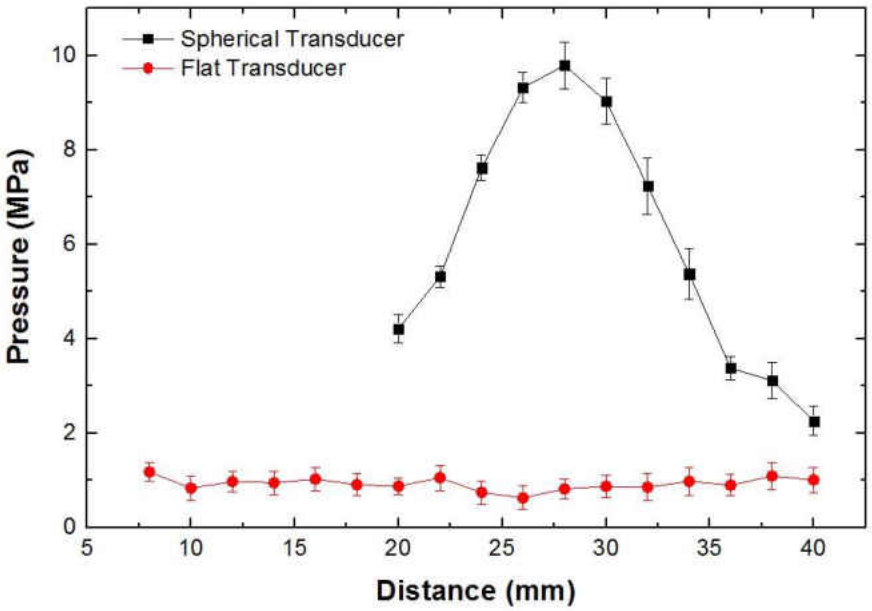

Figure 44. Pressure distribution for spherical and flat transducers.

7.1.3 Bubble Generation

To generate bubbles on the microscope, the chamber was placed under the objective lens (Figure 47). When the transducer was activated, a pressure wave was generated that oscillates at 2.1 MHz (Figure 43). Due to the compression and tension waves, microbubbles are generated and they quickly filled the chamber. In the chamber, a needle with a 190 μm diameter was placed to serve as a scale in Figure 46.

Under normal conditions, microbubbles or nuclei, are already present in the water. When the piezoelectric transducer is activated, the microbubbles oscillate in phase with the sound waves produced by the transducer. The bubbles expand under negative pressure and they contract under positive pressure. To characterize the growth of bubbles, a series of images was taken and analyzed. It was found that no bubble has a radius greater than 200 μm.

The bubbles at beginning are very small and hard to be seen. The inception of larger bubbles takes approximately 2-3 seconds. In one way, small bubbles become larger in size as time goes by. On the other hand, several small bubbles may merge and form single larger bubbles. Moreover, the bubbles may form clusters instead. As soon as the piezoelectric transducer was turned off, large bubbles were found to rise to the water surface.

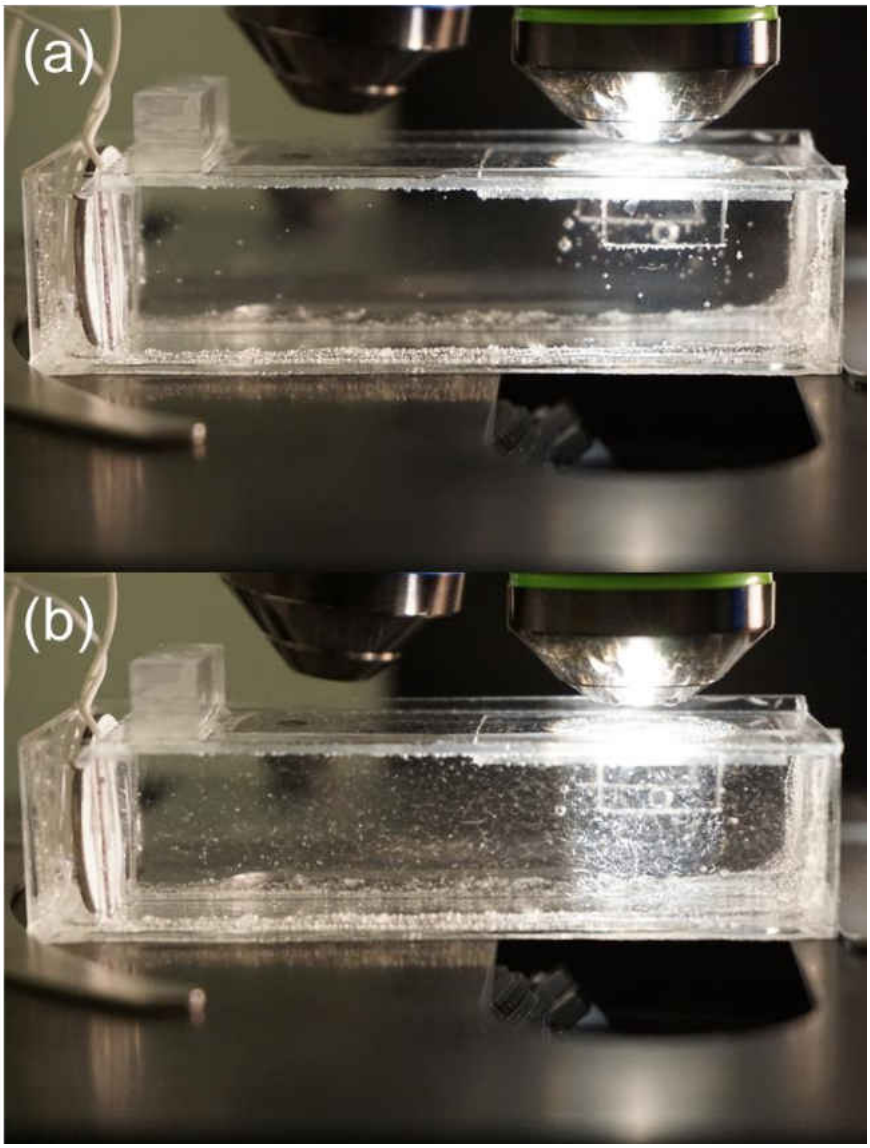

Figure 45. Snapshots of the chamber (a) before and (b) after bubble generation

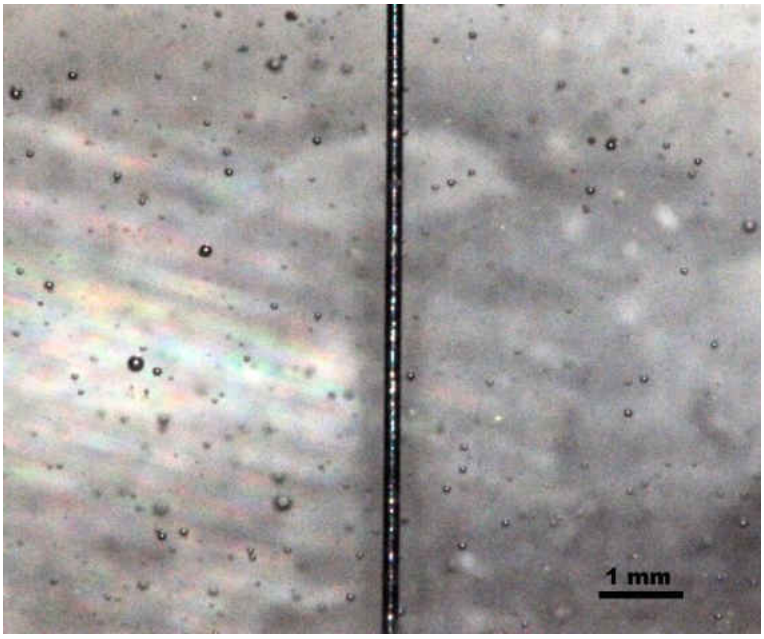

Figure 46. A still image of the microbubbles generated in tap water. A needle with a diameter of 190 µm was placed as a scale [30].

7.1.4 Bubbles on the Cover Slip

The cover slip in the chamber was carefully observed under the microscope and images were taken to analyze the bubbles on the surface of the cover slip. Before the device was activated (each trial), the lid and the coverslip were cleaned with an alcohol mix (IPA) and wiped with delicate task *KimWipes*®. The piezoelectric transducer's driver was set to run for 2 seconds and after 3 seconds, images were captured allowing the bubbles to rise to the surface of the chamber. During the capture of the images, larger bubbles were observed to rise to the surface (the glass lid in the chamber that also house the coverslip) and often, bubbles bonded together and rose to the surface as a unit. When the bubble clusters reached the surface, they sometimes stayed bonded, but often the bonded bubbles merged together and formed bigger bubbles as time passed by (Figure 47). It was also noted that smaller bubbles with radii less than 10 µm, rose to the surface before

the bigger bubbles settled, but they collapsed rather quickly as indicated by the arrow 2 in Figure 47.

There were 237 bubbles analyzed from the images by *ImageJ* which recognizes the bubbles and measure their dimensions based on the distance bar. The majority of these bubbles in terms of their radii fell between 10-30 µm, and bigger bubbles were less frequent to appear during the 2 seconds ON time analysis.

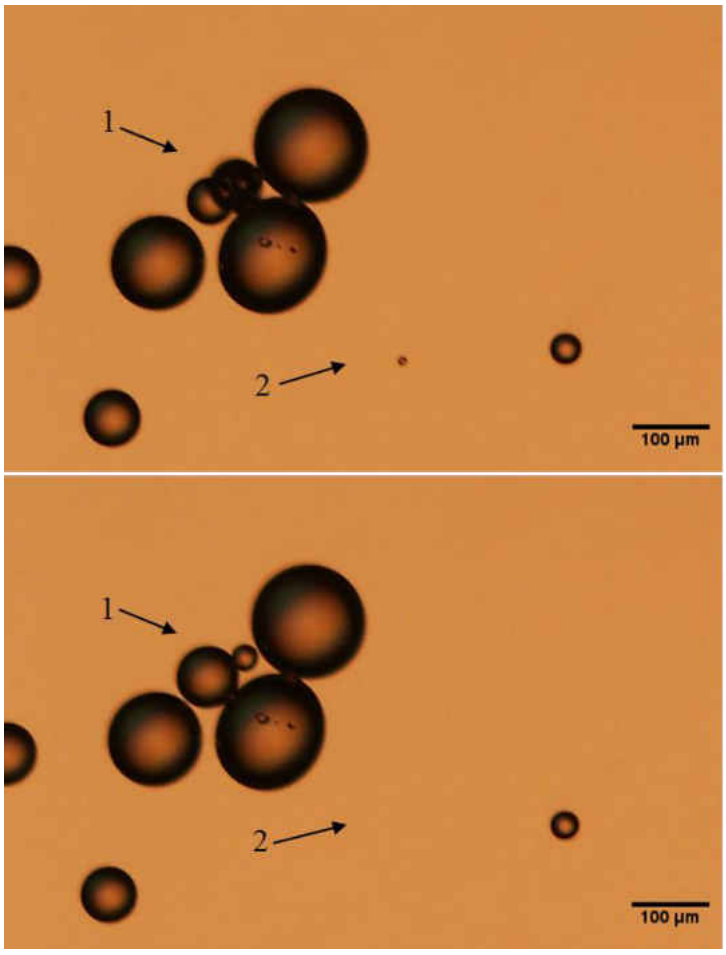

Figure 47. Two images captured within a second showing that bubbles cluster after reaching the cover slip.

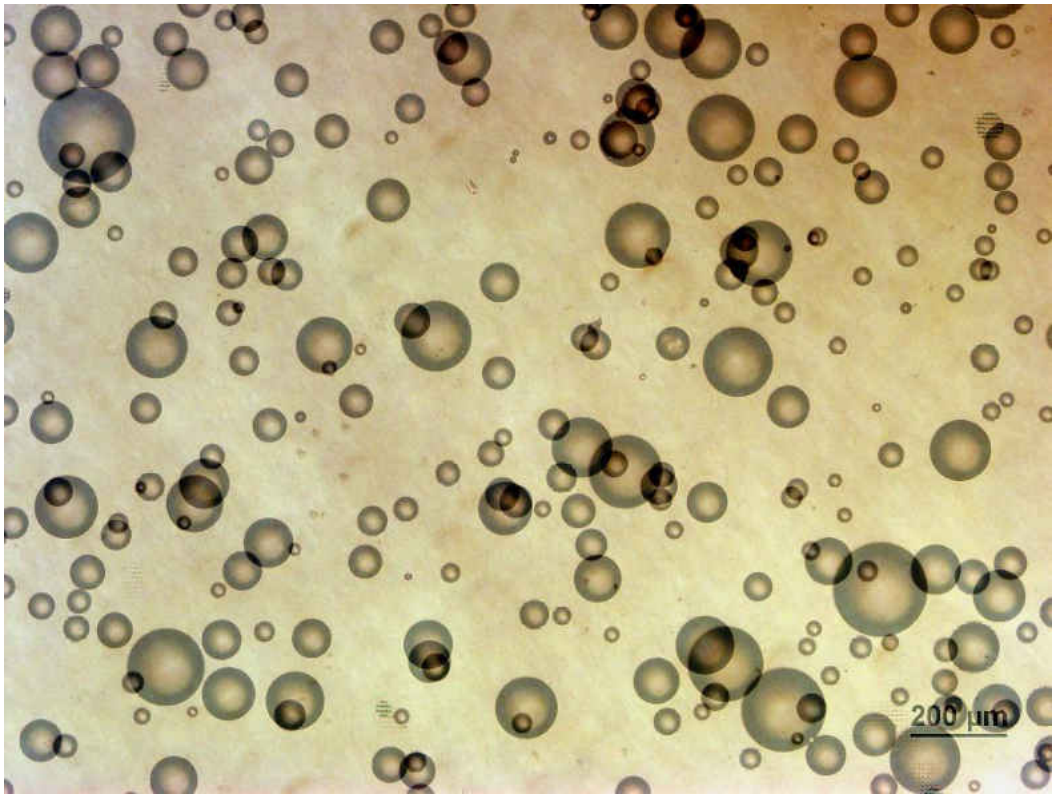

Figure 48. Summation of 17 images showing different bubble sizes.

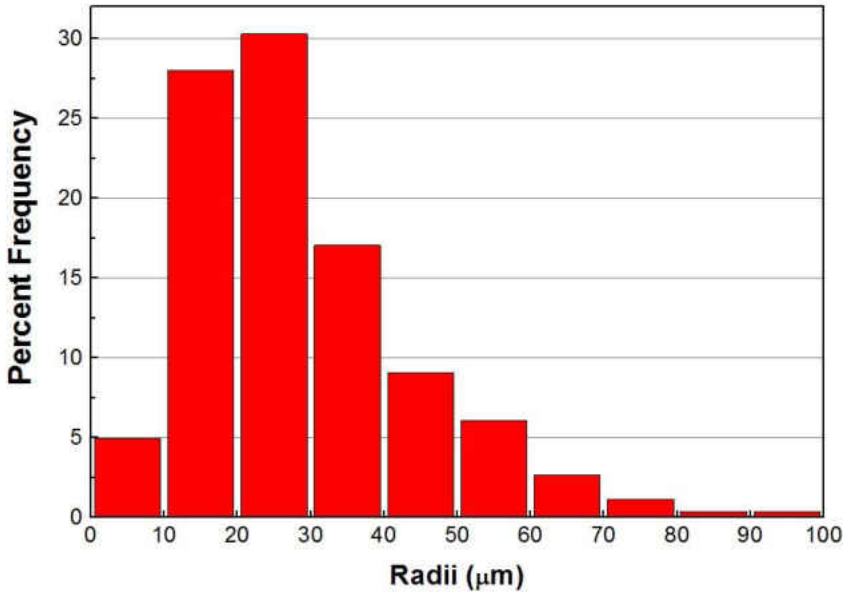

Figure 49. Histogram of the bubble radii of the superimposed image in figure 35.

To observe any correlation between the ON time and size of these bubbles, the system was left ON for 5, 10, 15, and 20 seconds. Consistently, the majority of the bubbles radii fell in the range of 10-30 µm, and no bubble with a radius larger than 200 µm was observed.

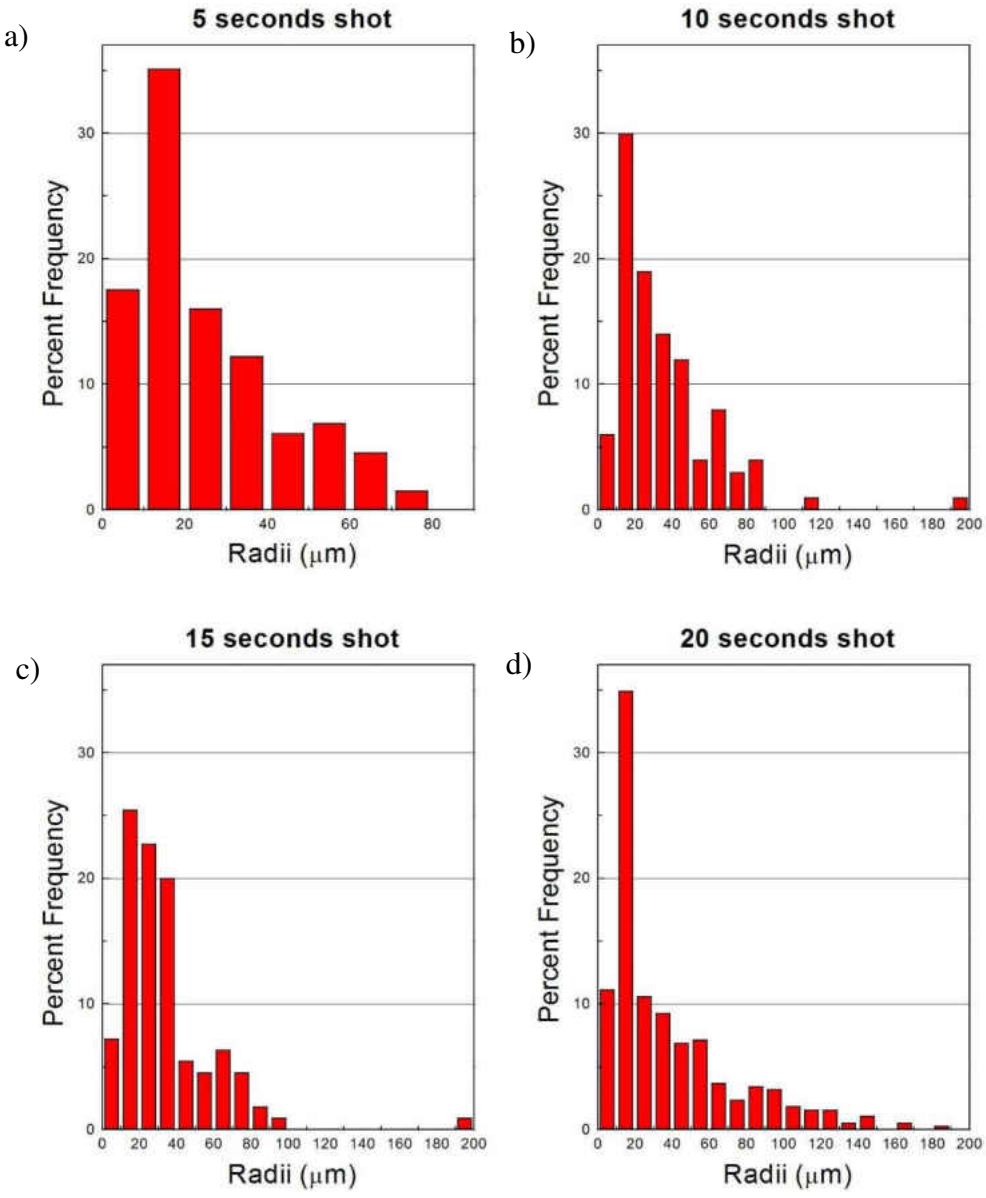

Figure 50. Histogram graphs for (a) 5 seconds shot, (b) 10 seconds shot, (c) 15 seconds shot, and (d) 20 seconds shot.

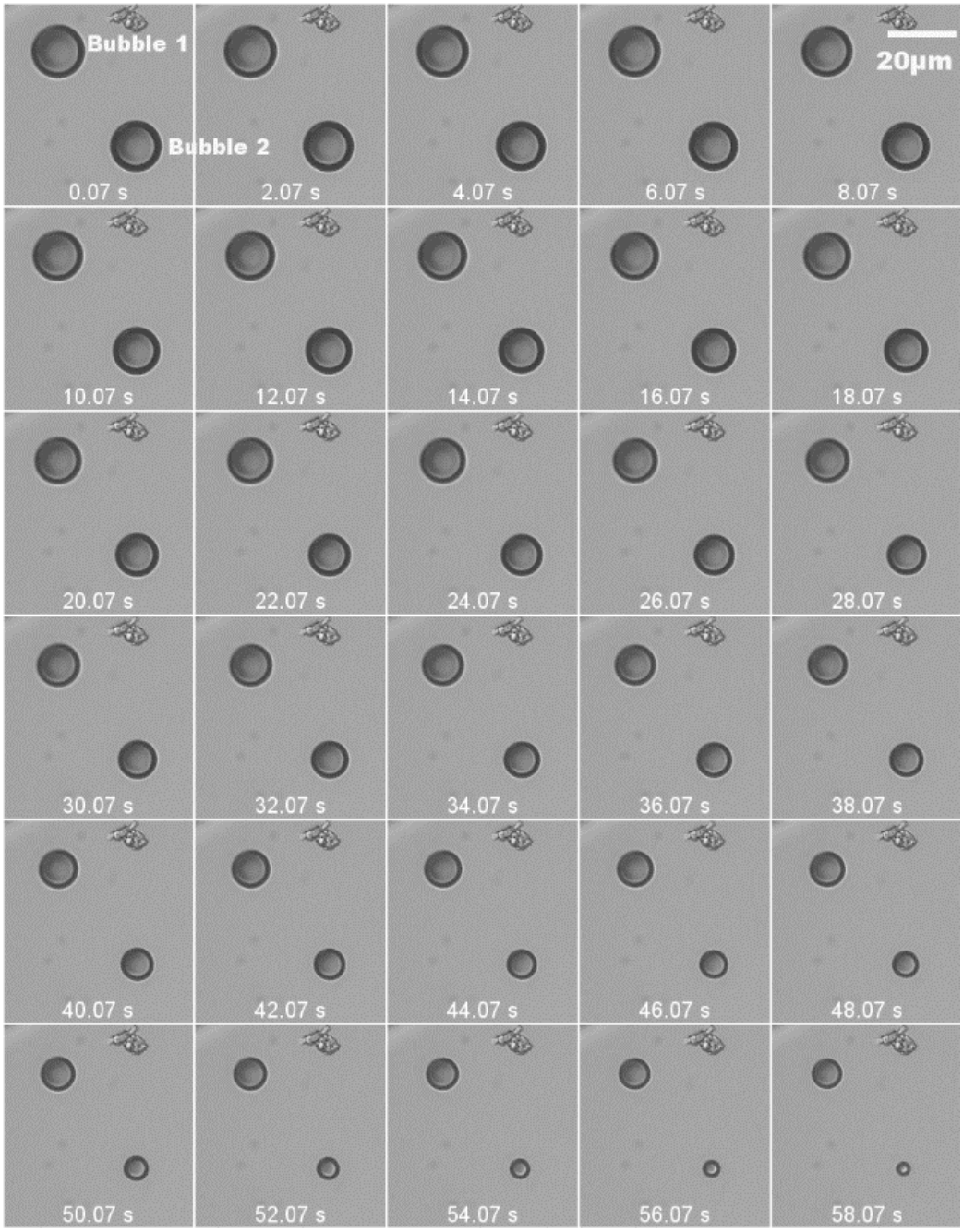

Figure 51. Photo montage of two bubbles collapsing at the surface of the chamber [30].

Though bubbles of similar size were often present, they may not collapse at the same rate. A series of 896 images of two similarly sized bubbles that were taken over 60 seconds were analyzed. Figure 51 shows a montage of the two bubbles. Figure 52 and Figure 53 show the two

bubbles collapsed at different speeds. In Figure 51, the first bubble had a 14 µm radius and the second bubble had a slightly smaller radius at 12.5 µm. Though the radios difference is not substantial, the calculated volume is 40% different. Observing the two bubbles, their radial collapsing speed is similar in the range of 14-8 µm, and beyond that range the second bubble collapsed faster than the first one, Figure 52 and Figure 53.

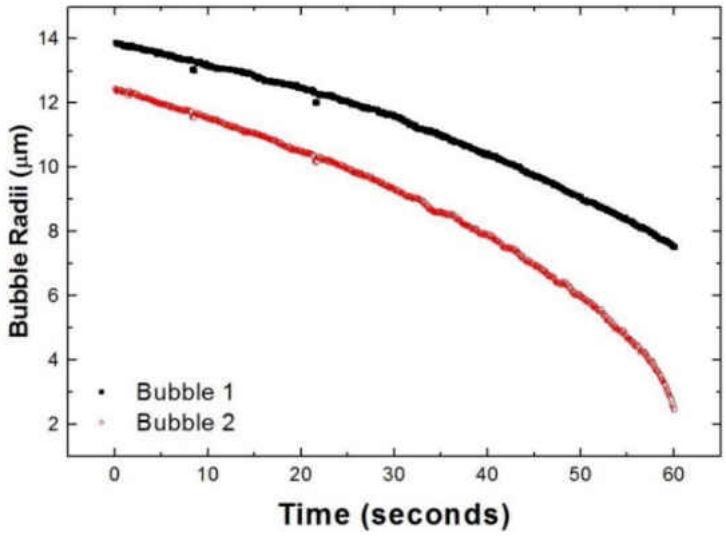

Figure 52. Time dependence of the radius of the cross-sectional circle [30].

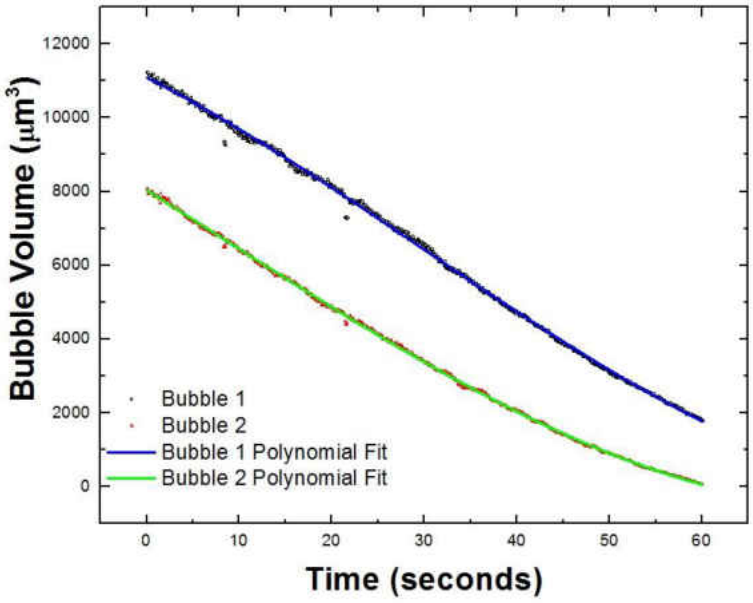

Figure 53. Time dependence of the evaluated bubbles' volumes [30].

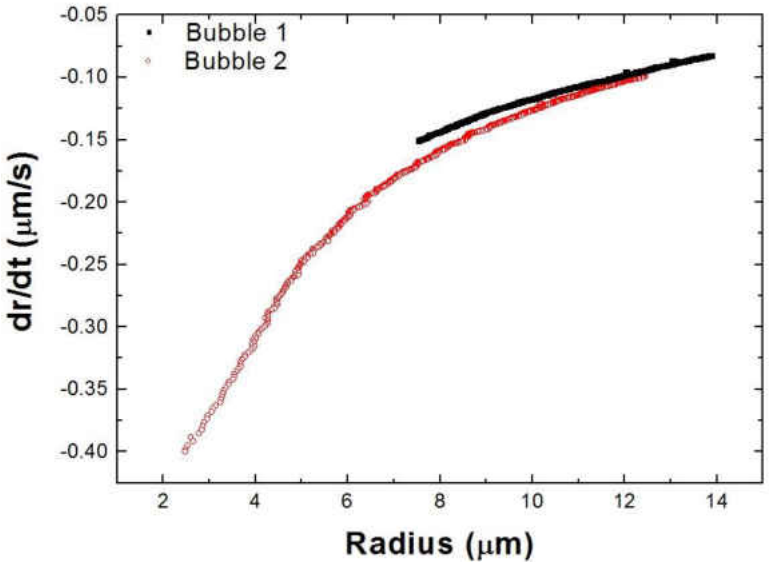

Figure 54. Radial collapsing speed versus the radius of the cross-sectional circle. As the bubble becomes smaller, the faster it collapses [30].

Through analyzing more images from the microscope, the large bubbles seem to contain what resembles condensed water. Figure 55 shows this phenomenon as the indicated object does not look like a bubble, but it looks like trapped water or even condensation as the bubbles themselves were initiated as steam. Though it is not clear whether the object found in the bubble is water or a bubble, from other images it's obvious that larger bubbles may have smaller bubbles adhered to its wall and if the smaller bubbles reached the cover slip first they might be embedded within the larger bubble as shown in Figure 56.

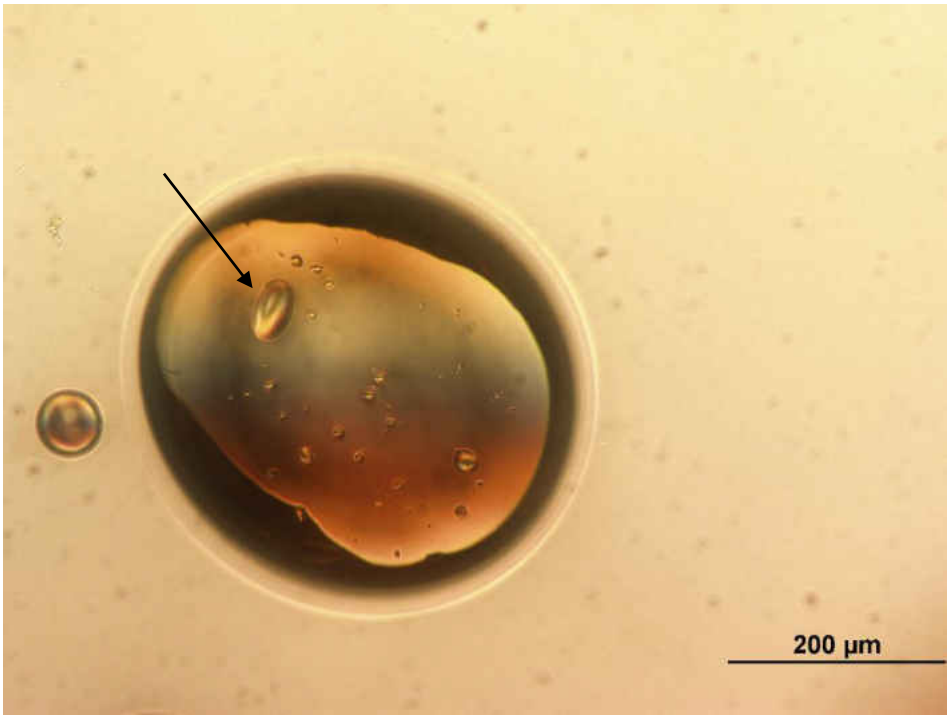

Figure 55. Condencation inside a bubble.

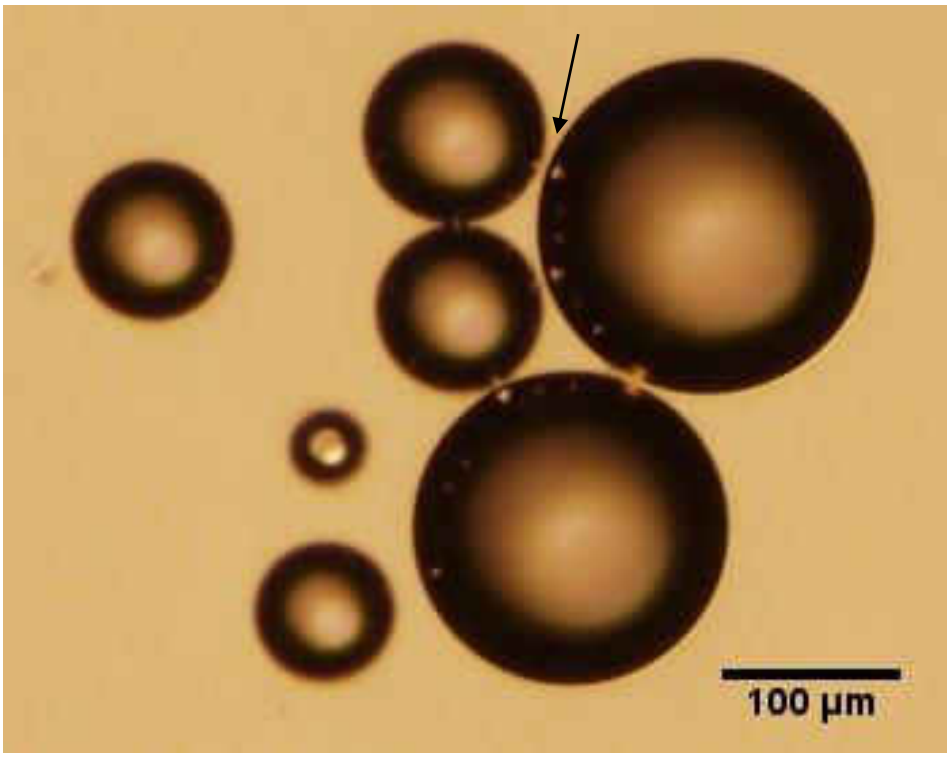

Figure 56. Smaller bubbles embedded in the walls of bigger bubbles.

CHAPTER 8

DISCUSSION

8.1 The Negative Impact of Increasing Driver Voltage

The original thought of producing pressure waves and shocks was that could use the push-pull driver to vary the voltage and pulse duration in a controlled manner. While the voltage (100V) was increased, a large amount of bubbles were able to be generated. But the side effect is that too high voltage could lead to the production of electrolysis bubbles. They can be observed visually like a smoke stemming from the transducer surface (Figure 57). Even when the driving pulse was reduced to 50 ms, the electrolysis was still observed. When the voltage was reduced to 60 V, the smoke was much less, but still present. After we switched to the self-resonance circuit, which has considerably lower voltage (~30 V), the electrolysis problem was eliminated.

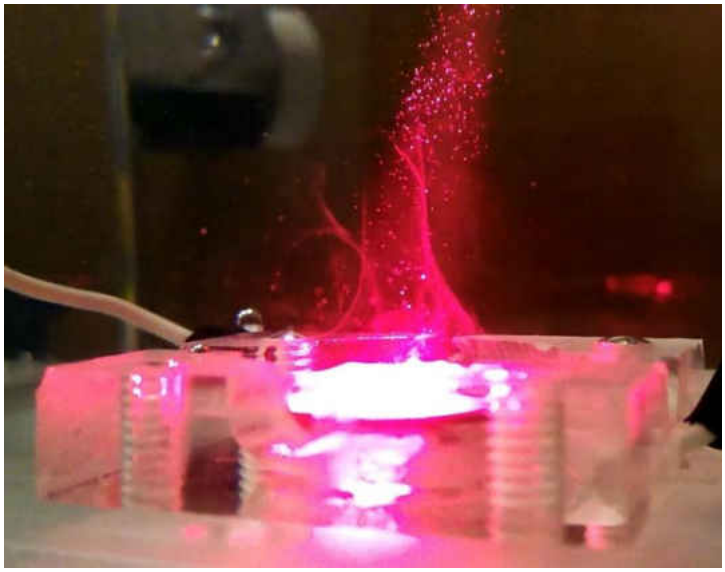

Figure 57. Electrolysis bubbles coming from a transducer after a 100 ms pulse.

8.2 The Choice of Driver's Frequency

The transducer of choice (SMD19T1112S) has a resonant frequency of 2.1 MHz and was chosen for three reasons:

1. Frequencies of ~20 kHz are known to generate large bubbles for mechanical shearing applications such as emulsification.
2. Frequencies within 100 kHz and 1 MHz are used to generate smaller bubbles for sonochemical purposes.
3. Frequencies greater than 1 MHz are known to have weaker cavitation effects but are commonly used for medical and imaging purposes.

By choosing 2.1 MHz transducer makes sense because power ultrasound is avoided while producing microbubbles for biological studies [30].

8.3 Bubble Growth

In water, gaseous impurities are present and they serve as the nuclei of bubble formation. In the event of negative pressure, water is pulled apart from the impurity sites, forming acoustic microbubbles. When water is subjected to positive pressure, these microbubbles are compressed, although not completely. In this system, the transducer delivers continuous acoustic pressure waves which means this process repeated in the following acoustic cycles of positive and negative pressures, and the cavitation bubbles formed grow accordingly, until they reach a critical size known as *resonance size*. Beyond that, the bubbles then might collapse violently or oscillate at or near the resonance size. Another possibility is that the bubbles may also split into smaller bubbles and reduce their sizes, which then serve as nuclei of new cavitation cycles. The relationship of the resonance radius of the bubble with the frequency f is given by Young [31] as

$$R_r = \sqrt{\frac{3\gamma p_\infty}{\rho\omega^2}} \tag{11}$$

where γ is the specific heat ratio of the gas inside the bubble, which is 1.33 for steam (water). p_∞ is the ambient liquid pressure, which is approximately considered as 1 atm. ρ is the liquid density, which is 999.97 kg/m^3 for water and ω is the angular frequency of the generated ultrasonic waves, which is $2\pi f = 1.32 \times 10^7$ Hz. The resonance radius is then evaluated to be about 1.52 μm. The resulting diameter of the bubbles is ~3 μm, which is beyond the detection range of the cameras used.

However, the growth of bigger bubbles beyond the resonance radiusR_r could be attributed to rectified diffusion and bubble coalescence. Rectified diffusion [32] is a nonlinear effect that involves an unequal mass transfer across the bubble interface in the rarefaction and compression phases of the ultrasound wave. From [33], it is suggested that gas diffusion into or out of a bubble depends on the surface area of the bubble. A bubble has a larger surface area during its expansion than its compression, therefore leading to more gas diffused into than out of the bubble. Also, the wall of a bubble thins during its expansion, making it easier for gas to diffuse in. One the other hand, coalescence involves multiple bubbles coming into contact with each other and forming wall partitions. The interface walls rupture when they become sufficiently thin, which leads to the formation of bigger bubbles [34].

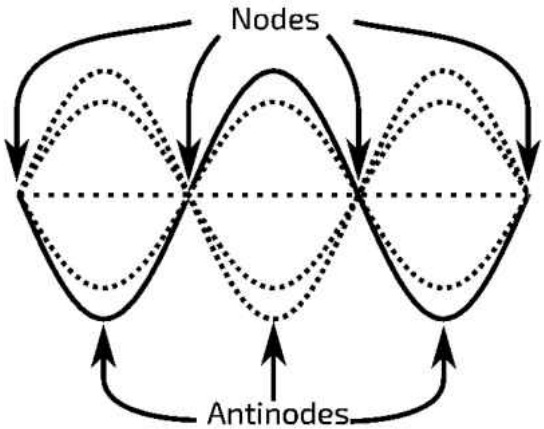

Figure 58. Nodes and antinodes of a sinusoidal standing wave [35].

The transducer is placed in one of the far ends of the glass chamber, reflected wave interfere with incoming waves, leads to nodes and antinodes of standing waves (Figure 58). Microbubbles formed at the antinodes that grow to a radius larger than R_r will be pushed toward the nodes by acoustic radiation forces on gas bubbles known as *primary Bjerknes forces* [36] and become inactive bubbles that do not implode violently within the liquid near the site of creation. These bubbles eventually become large enough and will rise to the surface the chamber due to their buoyancy after turning off the transducer.

Bubbles that rise to the surface of the chamber (coverslip) are of a radius distributed between 5 and 200 µm, and the majority of them have a radius between 10 and 30 µm. They gradually collapse on the cover slip or merge to form larger bubbles. Through visual observation, it was noticed that smaller a bubble is, the faster it collapses. It's believed that these bubbles are similar to the ones generated by the previous electrical discharges in water reported in [7] and [11]. The collapsing time of bubbles with initial radius of ~12 µm is observed to be about 60 s. This

long collapse time may be favored for biological studies where the observation of time evolution is of essence, [30].

CHAPTER 9

SUMMARY AND CONCLUSIONS

Bubble generation using piezoelectric transducers were studied. A curved transducer and a flat transducer were tested. Both of them can produce bubbles, but the flat one produced lower pressure intensity than the covered one. The curved transducer has an advantage in that the pressure wave can be focused at 30 mm from the transducer surface. It was found that it doesn't require very high voltage for these transducers to operate and one should be mindful of the electrolysis if too high voltage is applied. It is also important to create an environment where the standing wave can form, so that we are able to produce bubbles. This environment can be a chamber that allows a transducer to emit pressure sideway, so the pressure can bounce back from the opposing wall. A typical size of such chamber can be 8 cm × 2 cm × 2 cm. The driving frequency is critical to drive the transducer to produce the highest bubble yield.

The observations of the bubbles can be summarized as follows:

1. All bubbles collapse on the cover slip over time and the bubbles with a radius larger than 12 μm take more than 60 seconds to collapse.
2. Bubbles that are bonded together tend to combine (coalesce) and form a bigger bubble.
3. Larger bubbles may contain smaller bubbles.
4. Condensation might be present inside larger bubbles.

REFERENCES

[1] M. d'Agostino, C. K., E. Tibalt and R. S., "Shock wave as biological therapeutic tool: From mechanical stimulation to recovery and healing, through mechanotransduction," *International Journal of Surgery,* vol. 24, pp. 147-153, 2015.

[2] P. Lukes, P. Sunka, P. Hoffer, V. Stelmashuk, P. Pouckova, M. Zadinova, J. Zeman, L. Dibdiak, H. Kolarova, K. Tomankova, S. Binder and J. Benes, "Focused tandem shock waves in water and their potential application in cancer treatment," *Shock Waves,* vol. 24, no. 1, pp. 51-57, 2014.

[3] V. Menezes, K. Takayama, A. Gojani and S. H. R. Hosseini, "Shock wave driven microparticles for pharmaceutical applications," *Shock Waves,* vol. 18, pp. 393-400, 2008.

[4] J. J. Rassweiler, T. Knoll, K.-U. Köhrmann, J. A. McAteer, J. E. Lingeman, R. O. Cleveland, M. R. Bailey and C. Chaussy, "Shock Wave Technology and Application: An Update," *European Urology,* vol. 59, pp. 784-796, 2011.

[5] C. E. Brennen, *Cavitation and bubble dynamics*, Oxford, UK: Oxford University Press, 1995.

[6] X. Liu, Y. Luo and Z. Wang, "A review on fatigue damage mechanism in hydro turbines," *Renewable and Sustainable Energy Reviews,* vol. 54, pp. 1-14, 2016.

[7] S. Sun, J. Kanagari, L. Cho, D. Kang, S. Xiao and M. Cho, "Characterization of subcellular responses induced by exposure of microbubbles to astrocytes," *Journal of Neuotrauma,* vol. 32, no. 19, pp. 1441-1448, 2015.

[8] A. Nakagawa, G. T. Manley, A. D. Gean, K. Ohtani, R. Armonda, A. Tsukamoto, H. Yamamoto, K. Takayama and T. Tominaga, "Mechanisms of primary blast-induced traumatic brain injury: Insights from shock-wave research," *Journal of Neurotrauma,* vol. 28, pp. 1101-1119, 2011.

[9] J. V. Rosenfeld, A. C. McFarlane, P. Bragge, R. A. Armonda, J. B. Grimes and G. Ling, "Blast-related traumatic brain injury," *Lancet Neurol,* vol. 12, pp. 882-893, 2013.

[10] G. N. Sankin,, F. Yuan and P. Zhong, "Pulsating tandem microbubble for localized and directional single-cell membrane poration," *Physical Review Letters,* vol. 105, p. 078101, 2010.

[11] D. Kang, B. Nah, M. Cho and S. Xiao, "Shock wave generation in water for biological studies," *IEEE Transactions on Plasma Science,* vol. 42, no. 10, pp. 3231-3238, 2014.

[12] R. Zhao, R.-q. Xu and Z.-c. Liang, "Laser-induced plasma shock wave propagation underwater," *Optik,* vol. 124, pp. 1122-1124, 2013.

[13] V. Lazic and S. Jovićević, "Laser induced breakdown spectroscopy inside liquids: Processes and analytical aspects," *Spectrochimica Acta Part B: Atomic Spectroscopy,* vol. 101, pp. 288-311, 2014.

[14] B. Strycker, M. Springer, A. Traverso, A. Kolomenskii, G. Kattawar and A. Sokolov, "Femtosecond-laser-induced shockwaves in water generated at an air-water interface," *Optics Express,* vol. 21, no. 20, p. 23772, 2013.

[15] Y.-L. Ning and Y.-G. Zhou, "Shock tubes and blast injury modeling," *Chinese Journal of Traumatology,* vol. 18, pp. 187-193, 2015.

[16] Y. Chen and S. Constantini, "Caveats for using shock tube in blast-induced traumatic brain injury research," *Frontiers in Neurology,* vol. 4, 2013.

[17] J. Mankowski, "A review of short pulse generator technology," *IEEE Transactions on Plasma Science,* vol. 28, no. 1, pp. 102-108, 2000.

[18] S. Katzir, "Introduction," in *The Beginnings of Piezoelectricity: A Study in Mundane Physics*, Berlin, Heidelberg, Springer Science & Business Media, 2007, pp. 1-13.

[19] X. Zhu, Piezoelectric Ceramic Materials : Processing, Properties, Characterization, and Applications, New York: Nova Science Puplishers, Inc, 2010.

[20] noliac, "noliac," [Online]. Available: http://www.noliac.com/fileadmin/user_upload/documents/Tutorials/Tutorials_Manufacturing.pdf. [Accessed 4 8 2015].

[21] W. P. Mason, "Nature of piezoelectric effect," in *Piezoelectric Crystals and Their Application to Ultrasonics*, Princeton, New Jersey, D. van Nostrand Company, Inc., 1950, p. 1.

[22] Pinin, "Wikipedia," [Online]. Available: https://commons.wikimedia.org/wiki/File:Perovskite.svg#/media/File:Perovskite.svg. [Accessed 15 7 2015].

[23] S. Sherrit, H. D. Wiederick, B. K. Mukherjeey and M. Sayer, "An accurate equivalent circuit for the unloaded piezoelectric vibrator in the thickness mode," *Journal of Physics D: Applied Physics,* vol. 30, no. 16, p. 2354–2363, 1997.

[24] J. Kim, B. L. Grisso, J. K. Kim, D. S. Ha and D. J. Inman, "Electrical modeling of piezoelectric ceramics for analysis and evaluation of sensory systems," in *IEEE Sensors Applications Symposium*, Atlanta, GA, 2008.

[25] IEEE Std 177, "IEEE Standard Definitions and Methods of Measurement for Piezoelectric Vibrators," 1966.

[26] PCB Piezotronics, Inc., "Model 113B24 ICP® Pressure Sensor Installation and Operating Manual," PCB Piezotronics, Inc., Depew, NY, 2013.

[27] *Release on the Refractive Index of Ordinary Water Substance,* Erlangen: International Association for the Properties of Water and Steam, 1997.

[28] *Release on the IAPWS Formulation 1995 for the Thermodynamic Properties of Ordinary Water Substance for General and Scientific Use,* Fredericia: The International Association for the Properties of Water and Steam , 1996.

[29] ONDA, "HFO-690 Fiber Optic Hydrophone User's Manual," Sunnyvale, CA, 2014.

[30] W. Zhu, M. Alkhazal, M. Cho and S. Xiao, "Microbubble generation by piezotransducer for biological studies," *Review of Scientific Instruments,* vol. 86, p. 124901, 2015.

[31] F. R. Yong, *Cavitation*, London: McGraw-Hill, 1989.

[32] D.-Y. Hsieht and M. S. Plesset, "Theory of rectified diffusion of mass into gas bubbles," *The Journal of the Acoustical Society of America,* vol. 33, no. 2, pp. 206-215, 1961.

[33] A. Eller and H. G. Flynn, "Rectified diffusion during nonlinear pulsations of cavitation bubbles," *The Journal of the Acoustical Society of America,* vol. 37, no. 3, pp. 493-503, 1965.

[34] M. Ashokkumar, J. Lee, S. Kentish and F. Grieser, "Bubbles in an acoustic field: An overview," *Ultrasonics Sonochemistry,* vol. 14, no. 4, pp. 470-475, 2007.

[35] "Isaac Physics," [Online]. Available: https://isaacphysics.org/concepts/cp_standing_waves. [Accessed 15 3 2016].

[36] T. G. Leighton, A. J. Walton and M. J. W. Pickworth, "Primary Bjerknes forces," *European Journal of Physics,* vol. 11, no. 1, pp. 47-50, 1990.

[37] W. Mason, *Physical acoustics and the properties of solids*, New York: D. VAN nostrand company, INC, 1958.

[38] J. Yang, *Vibration of piezoelectric crystal plates*, New Jersey: World Scientific Publishing Company, 2013.

[39] N. Pérez, F. Buiochi, M. A. B. Andrade and J. C. Adamowski, "Numerical Characterization of Piezoceramics Using Resonance Curves," *Materials,* vol. 9, no. 2, pp. 1-30, 2016.

[40] V. Piefort, "Universite Libre de Bruxelles," 2001. [Online]. Available: http://scmero.ulb.ac.be/Publications/Thesis/Piefort01.pdf. [Accessed 30 7 2015].

[41] P. D. e. al., "Chapter 2 Piezoelectric materials," in *Dynamic Fracture of Piezoelectric Materials, Solid Mechanics and Its Applications*, Springer International Publishing Switzerland, 2014.

[42] W. Mason, *Piezoelectric crystals and their application to ultrasonics*, New York: D. van Nostrand Company, Inc, 1950.

[43] J.-P. Franc and J.-M. Michel, *Fundamentals of cavitation*, Dordrecht: Kluwer academic publishing, 2004.

APPENDIX A

PIEZOELECTRICY CONSTITUTIVE EQUATIONS AND COEFFICIENTS

A.1. Constitutive Equations

Modeling piezoelectric materials came about from the principles of thermodynamics because the mechanical and electrical variables of piezoelectric materials are coupled. Essentially piezoelectric material is treated as closed system so that its internal energy change can be quantified. Moreover, different thermodynamic potentials are used to derive the model with different natural variables (independent variables). The information presented in this report follows IEEE standards for piezoelectric constitutive equations. First, we define the mechanical stress for an elastic body using Hooke's law as follows,

$$T = cS \tag{12}$$

where T is the stress, c is the stiffness, and S is the strain of the material. The strain of a material is given by the percentage of elongation of the material under stress. The direct piezoelectric effect is a result of induced polarization eS proportional to the strain so that the polarization expression becomes:

$$P = (\varepsilon - \varepsilon_0)E + eS \tag{13}$$

The polarization is related to the electric displacement as:

$$D = \varepsilon_0 E + P \tag{14}$$

The direct or inverse piezoelectric effect is also proportional to the electric field as it induces stress $-eE$ where e is a piezoelectric constant that is expressed in $\mathrm{N/Vm}$ and it relates the charge

per unit area and zero electric field strain. Finally, the electromechanically coupled equations become the following:

$$D = eS + \varepsilon^S E \tag{15}$$

$$T = c^E S - eE \tag{16}$$

where D is the electric displacement, c^E is the stiffness at a constant electric field and ε^S is the permittivity at constant strain. Equations (9) and (10) are derived from the three forms of work that establishes the variation of stored internal energy dU. The works of mechanical forces, electric field and thermal energy are considered and the expression for dU is:

$$dU = TdS + EdD + \theta d\varsigma \tag{17}$$

where θ is the temperature. The natural variables are the strain S, electric displacement D, and the entropy ς. Note that the electric displacement is related to the polarization of the material and the electric field as follows:

$$D = \varepsilon_0 E + P \tag{18}$$

Also, note that the variable θ is the temperature. To write the constitutive equations using the strain, electric field, and temperature as independent variables, the differential forms of the dependent variables, which are stress, electric displacement, and entropy:

$$dT = \frac{\partial T}{\partial S} dS + \frac{\partial T}{\partial E} dE + \frac{\partial T}{\partial \theta} d\theta \tag{19}$$

$$dD = \frac{\partial D}{\partial S} dS + \frac{\partial D}{\partial E} dE + \frac{\partial D}{\partial \theta} d\theta \tag{20}$$

$$d\varsigma = \frac{\partial \varsigma}{\partial S} dS + \frac{\partial \varsigma}{\partial E} dE + \frac{\partial \varsigma}{\partial \theta} d\theta \tag{21}$$

All of equation (19), (20), and (21) are to define important relationships to the physical meaning of the equations, and how they are related, table A1.

Table A1. Physical meaning of the partial derivatives of the internal energy

$\frac{\partial T}{\partial S} = c$ elasticity	$\frac{\partial T}{\partial E} = e$ inverse piezoelectricity	$\frac{\partial T}{\partial \theta} = \lambda$ thermal stress
$\frac{\partial D}{\partial S} = e$ direct piezoelectricity	$\frac{\partial D}{\partial E} = \varepsilon$ permittivity	$\frac{\partial D}{\partial \theta} = p$ pyroelectricity
$\frac{\partial \varsigma}{\partial S} = \lambda$ piezocaloric effect	$\frac{\partial \varsigma}{\partial E} = p$ electrocaloric effect	$\frac{\partial \varsigma}{\partial \theta} = \alpha$ heat capacity

Now introduce Gibbs electric function (also called thermoelectric Gibbs free energy) to fully describe the system thermodynamically,

$$G_2 = U - ED - \theta\varsigma \tag{22}$$

Its deferential form is,

$$dG_2 = TdS - DdE - \varsigma d\theta \tag{23}$$

as a result,

$$T = \frac{\partial G_2}{\partial S} \tag{24}$$

$$D = -\frac{\partial G_2}{\partial E} \tag{25}$$

$$\varsigma = -\frac{\partial G_2}{\partial \theta} \tag{26}$$

Second order partial derivatives of stress and displacement of Equation (22) with respect to E and θ leads to the following:

$$\frac{\partial T}{\partial E} = \frac{\partial G_2}{\partial S \partial E} = -\frac{\partial D}{\partial S} \tag{27}$$

$$\frac{\partial T}{\partial \theta} = \frac{\partial G_2}{\partial S \partial \theta} = -\frac{\partial \varsigma}{\partial S} \tag{28}$$

$$\frac{\partial D}{\partial \theta} = -\frac{\partial G_2}{\partial E \partial \theta} = \frac{\partial \varsigma}{\partial E} \tag{29}$$

One can draw the conclusion that the coefficient for the direct and inverse piezoelectric effects from Equation (27).

The equation for free energy is:

$$A = U - TS \tag{30}$$

Using Equations (22), (24), (25), (26) and Table A1, one gets the following equations:

$$T = c^E S - eE - \lambda\theta \tag{31}$$

$$D = eS + \varepsilon^S E + p\theta \tag{32}$$

$$\varsigma = \lambda S + p^S E + \alpha\theta \tag{33}$$

Neglecting the heat effects per IEEE standards, equation (33) is disregarded, and the heat related terms in (31) and (32) are omitted and the results are the same equations in (15) and (16).

A.2. Characterization of Thickness Vibration Mode Piezoceramics

Piezoelectric material such as piezoceramics e.g. PZT are anisotropic materials and as a consequence true modeling has to be done with tensor relations because the physical parameters are directional. For example, the stress that is applied to a cubic unit cell has three components on each face along the three space axis x, y, and z. Going through these in details is beyond the purpose of this thesis but one can visit books such as Mason [21] and [37], also Yang [38]. However, since thickness vibration mode piezoelectric ceramics were used in this work, a brief characterization of these transducers is due.

A thickness vibration mode piezoelectric transducer is a device that is manufactured as plates, rings, or discs. In this work, piezoceramic discs were used and for these devices, the piezoelectric properties are built in along its thickness by the poling process. The poling process takes place when the raw piezoelectric material is mixed and machined into the final shape desired. A high electric field is applied at the electrodes resulting into an axis specific transducer device by properly orienting the polarization domains in the material, see Figure 59. This poling process determines the vibration mode of a piezoceramic transducer such as radial, longitudinal, or thickness as in Figure 9.

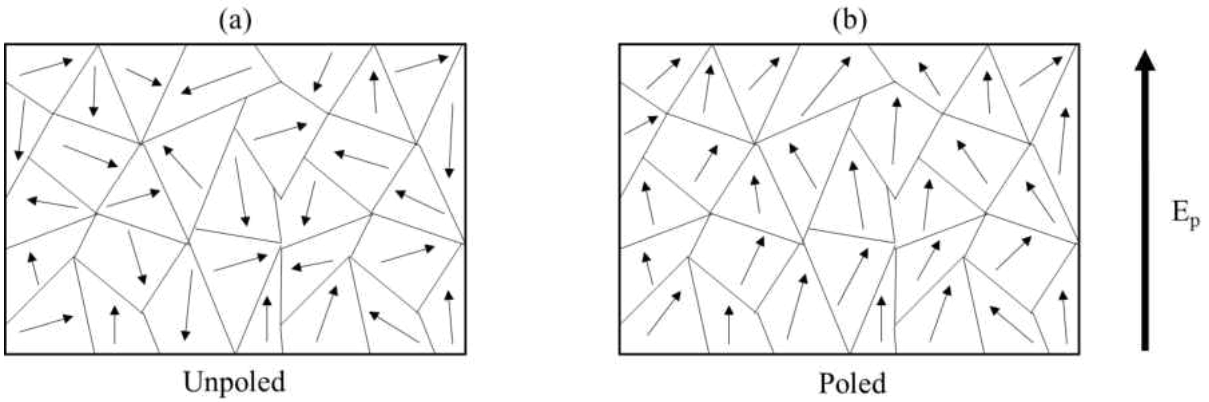

Figure 59. The effect of poling on polarization domains. (a) Unpoled (b) Poled.

Since a thickness vibration mode piezoceramic is piezoelectric only along its thickness axis, one-dimensional modeling is acceptable [39]. In tensor convention x, y, and z are expressed as 1, 2, and 3, as shown in Figure 60. Directional coefficients will have subscripts denoting the direction associated with the physical effect, Table A2.

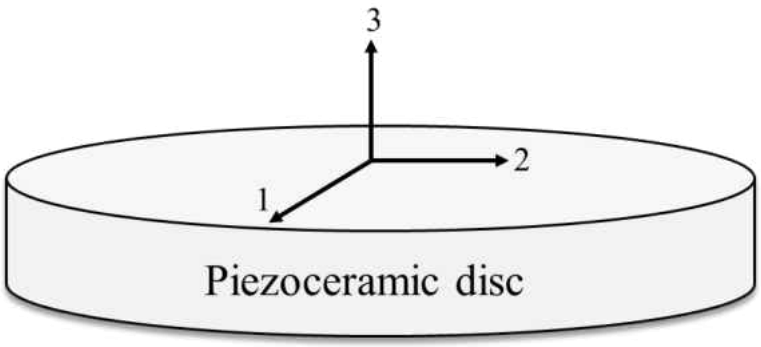

Figure 60. One-dimensional model of a thickness vibration mode piezoceramic.

Table A2. Piezoceramic discs characterizing coefficients (Thickness vibration mode)

Property	**Symbol(s)**	**Unit**
Electromechanical coupling coefficients	k_t, k_{31}	-----
Frequency constants	N_t	Hz·m
Piezoelectric charge constants Piezoelectric voltage constants	d_{33}, d_{31} g_{33}, g_{31}	m/V Vm/N
Young's modulus	Y_{33}, Y_{31}	N/m^2
Elastic stiffness	c_{33}	N/m^2
Mechanical quality factor	Q_m	-----
Curie temperature	T_c	˚C
Density of the material	ρ	g/cm^3

k_{31} is the electmechanical coupling coefficient of the electric field in direction 3 and the mechanical vibration in direction 1. k_t , refers to the coupling along the thickness. N_t is the frequency constant with respect to the thickness of the piezoceramic and its resonance frequency. The piezoelectric constants (d_{ij} and g_{ij}) are found in the following tensor relations:

$$S_{ij} = d_{ij}E_k \tag{34}$$

$$g_{ij} = -\frac{\partial E_i}{\partial T_j} \tag{35}$$

The Young's modulus is the ration between the stress applied and resulted strain. The elastic stiffness describes the linear relationship between the stress and strain and given by the following tensor relation (generalized Hooke's law):

$$T_i = c_{ij} S_j \tag{36}$$

The mechanical quality factor is:

$$Qm = 2\pi \frac{stored\ mechanical\ energy\ at\ resonance}{mechanical\ disspated\ energy\ per\ resonant\ cycle} \tag{37}$$

and the Curie temperature is the temperature at which the material cannot maintain polarization and the net polarization goes to zero, thus the piezoelectric effects are no longer in effect.

VITA

Mohammed Alkhazal
4233 Llewellyn Ave APT# 306 Norfolk, VA | malkh006@odu.edu | 804-503-8888

Senior Design Project Old Dominion University (2014)
Design of High Voltage Nanosecond Pulse Generator
Lab assistant at Frank Reidy Research Center for Bioelectrics. (2014-2016)
Simulation: PSpice – OrCAD Capture.
Pressure measurement using fiber optic pressure transducer, ONDA HFO-690.

OLD DOMINION UNIVERSITY, Norfolk, VA
B.S. Electrical Engineering (December 2014)
GPA 3.51
Dean's List
Relevant Course Work:
Electromagnetism, Electric Drives, Power Electronics, Control Systems Instrumentation (LabVIEW)

OLD DOMINION UNIVERSITY, Norfolk, VA
M.S. Electrical Engineering (August 2016)
GPA 3.82
Relevant Course Work:
Lasers, Fiber Optic Communication, Plasmas, Material and Surface Science, Material Characterization, Solar Cells, Piezoelectricity

PUBLICATIONS:

Generating focused pressure wave with ultrasound piezotranducers, 2015 IEEE Pulsed Power Conference (PPC) DOI:10.1109/PPC.2015.7296924

Microbubble generation by piezotransducer for biological studies, Review of Scientific Instruments 86, 124901 (2015); DOI: 10.1063/1.4936555